Cell Reports

Article

hnRNPA2B1 represses the disassembly of arsenite-induced stress granules and is essential for male fertility

Graphical abstract

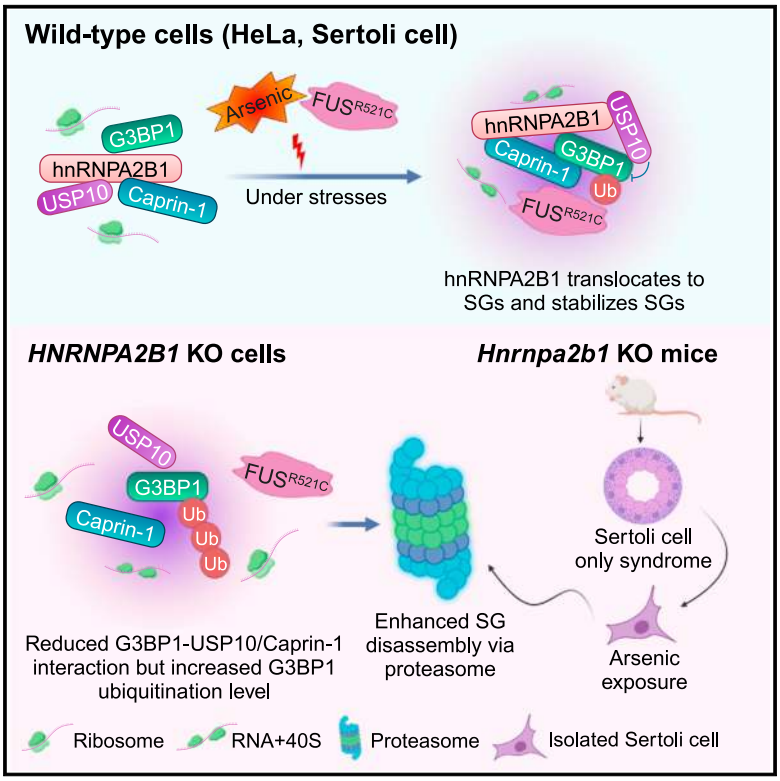

Highlights

- hnRNPA2B1 associates with SGs and interacts with several SG core proteins
- hnRNPA2B1 depletion accelerates SG disassembly via the ubiquitination-proteasome system
- hnRNPA2B1 regulates the G3BP1-USP10 interaction and USP10 can deubiquitinate G3BP1
- Male *Hnrnpa2b1* knockout mice are infertile due to Sertoli cell-only syndrome

Authors

Xiaoli Wang, Xu Fan, Jin Zhang, ..., Heng Gu, Youzhi Zhang, Shuiqiao Yuan

Correspondence

wangxiaoli@hust.edu.cn (X.W.), shuiqiaoyuan@hust.edu.cn (S.Y.)

In brief

Wang et al. find that hnRNPA2B1 can translocate to stress granules (SGs) under various stresses, interact with several SG core proteins, and stabilize SGs. hnRNPA2B1 deletion promotes SG disassembly in both HeLa and mouse Sertoli cells under arsenic stress, and hnRNPA2B1 is essential for spermatogenesis in mice.

Wang et al., 2024, Cell Reports *43*, 113769
February 27, 2024
https://doi.org/10.1016/j.celrep.2024.113769

CellPress

Cell Reports

CellPress
OPEN ACCESS

Article

hnRNPA2B1 represses the disassembly of arsenite-induced stress granules and is essential for male fertility

Xiaoli Wang,[1,6,*] Xu Fan,[1,6] Jin Zhang,[1,6] Fengli Wang,[1,6] Jingshou Chen,[1] Yujiao Wen,[1] Lingjuan Wang,[1] Tao Li,[1] Huaibiao Li,[1] Heng Gu,[2] Youzhi Zhang,[3] and Shuiqiao Yuan[1,4,5,7,*]

[1]Institute of Reproductive Health, Tongji Medical College, Huazhong University of Science and Technology, Wuhan 430030, China
[2]NHC Key Laboratory of Male Reproduction and Genetics, Guangdong Provincial Reproductive Science Institute (Guangdong Provincial Fertility Hospital), Guangzhou 510600, China
[3]School of Pharmacy, Hubei University of Science and Technology, Xianning 437100, China
[4]Laboratory of the Animal Center, Huazhong University of Science and Technology, Wuhan 430030, China
[5]Shenzhen Huazhong University of Science and Technology Research Institute, Shenzhen 518057, China
[6]These authors contributed equally
[7]Lead contact
*Correspondence: wangxiaoli@hust.edu.cn (X.W.), shuiqiaoyuan@hust.edu.cn (S.Y.)
https://doi.org/10.1016/j.celrep.2024.113769

SUMMARY

Although the composition and assembly of stress granules (SGs) are well understood, the molecular mechanisms underlying SG disassembly remain unclear. Here, we identify that heterogeneous nuclear ribonucleoprotein A2/B1 (hnRNPA2B1) is associated with SGs and that its absence specifically enhances the disassembly of arsenite-induced SGs depending on the ubiquitination-proteasome system but not the autophagy pathway. hnRNPA2B1 interacts with many core SG proteins, including G3BP1, G3BP2, USP10, and Caprin-1; USP10 can deubiquitinate G3BP1; and hnRNPA2B1 depletion attenuates the G3BP1-USP10/Caprin-1 interaction but elevates the G3BP1 ubiquitination level under arsenite treatment. Moreover, the disease-causing mutation FUS^{R521C} also disassembles faster from SGs in *HNRNPA2B1* mutant cells. Furthermore, knockout of hnRNPA2B1 in mice leads to Sertoli cell-only syndrome (SCOS), causing complete male infertility. Consistent with this, arsenite-induced SGs disassemble faster in *Hnrnpa2b1* knockout (KO) mouse Sertoli cells as well. These findings reveal the essential roles of hnRNPA2B1 in regulating SG disassembly and male mouse fertility.

INTRODUCTION

In eukaryotic cells, one of the mechanisms in response to environmental and biotic stress, such as heat shock, oxidative stress, viral infection, osmotic stress, UV irradiation, or cold shock, is the formation of stress granules (SGs), non-membranous cytoplasmic aggregates containing mRNA and protein. Although SGs were originally thought to be sites of translational repression, recent studies have shown that the formation of visible SGs may not be required for efficient translation shutdown.[1,2] These carefully controlled subcellular structures are considered to originate through liquid-liquid phase separation (LLPS) of low-complexity protein domains and are highly conserved. The physics of LLPS underlying the development of SGs have demonstrated that there is a network of linked SG regulator proteins, with G3BP1 acting as the central node.[3–5] SGs are signaling hubs that coordinate cell growth and metabolism in response to environmental changes, thereby allowing cells to adapt to stressors.[6] Numerous diseases are linked to improper SG management, ranging from aging to neurodegenerative illnesses.[7,8] While the mechanisms of SG assembly in response to different stressors have been extensively studied in various model systems, the mechanisms under SG disassembly have so far evaded us to a great extent.

As a temporary adaptive stress response, SGs promptly deconstruct when the initial stress is removed in a context-dependent mechanism depending on the type and duration of the initiating stress, mainly through the autophagy pathway and/or ubiquitination-proteasome system. Short-lived SGs remain dynamic and are quickly eliminated by decondensation (a reversal of LLPS), allowing constituents to be recycled.[9] On the other hand, persistent SGs, such as chronic stress or disease-related mutations, are cleared by autophagy-dependent degradation,[10,11] leading to the degradation and permanent loss of constituent proteins and RNAs. In the case of SG context, cells employ different signaling pathways to disassemble SGs. The disassembly of heat-shock-induced SGs is much more dependent on ubiquitination than arsenite-induced SGs, although ubiquitination occurs under both stresses.[10–12] In addition, defective SG disassembly and their development into

aggregates are promoted by persistent stress and mutations in RNA binding proteins (RBPs), such as TDP-43, FUS, and hnRNPA1, associated with neurodegenerative disorders.[13–15]

Heterogeneous nuclear ribonucleoprotein A2/B1 (hnRNPA2B1) is an RBP, and it regulates RNA metabolism in a variety of ways, including mRNA processing,[16] microRNA (miRNA) processing[17] and exosomal sorting,[18] mRNA decay,[19] telomere maintenance,[20] transcript stability,[21] translational control,[22] and innate immune response.[23] Notably, after arsenite treatment, both wild-type hnRNPA2 and pathogenic mutant hnRNPA2 (D290V) can localize in SGs, and hnRNPA2 (D290V) is incorporated into SGs faster than wild-type (WT) hnRNPA2.[24] Notably, hnRNPA2 (D290V) results in increased muscle degeneration, which correlates with increased cytoplasmic inclusion formation.[24] It has been proposed that the D290V mutation located in the center of the prion-like domain (PrLD) and is expected to increase prion susceptibility. Most strikingly, the D290V mutation causes a mutant hexapeptide to become highly amyloidogenic, whereas the WT peptide is not.[25] These findings suggest a link between hnRNPA2B1 and SGs; however, the role of hnRNPA2B1 in the SG dynamic process is still unknown.

Here, we report that hnRNPA2B1 depletion in HeLa cells accelerates SG disassembly relying on the ubiquitination-proteasome system but not the autophagy pathway and enhances the disassembly of the pathological mutation FUS^{R521C} from arsenite-induced SGs. Additionally, hnRNPA2B1 interacts with G3BP1 through its C-terminal domain and regulates G3BP1-USP10 interaction intensity and the ubiquitination level of G3BP1 under arsenite stress. Further, we generated *Hnrnpa2b1* knockout (KO) mice and found that the KO males are completely sterile, accompanied by Sertoli cell-only syndrome (SCOS), and showed that arsenite-induced SGs were disassembled faster as well in mouse *Hnrnpa2b1* KO Sertoli cells. We demonstrate that hnRNPA2B1 regulates SG disassembly and is essential for male fertility in mice.

RESULTS

hnRNPA2B1 localizes with SGs upon various stresses

To elucidate the cellular function of hnRNPA2B1 during SG assembly, we examined the subcellular localization of hnRNPA2B1 under conditions with or without arsenite treatment. hnRNPA2B1 was mainly diffusely localized in the nucleus under the untreated condition, whereas arsenite treatment induced its accumulation in cytoplasmic SGs (Figure 1A). hnRNPA2B1 could localize to SGs under arsenite with different concentrations (0.02 mM, 0.05 mM, 0.10 mM, 0.25 mM, and 0.50 mM; Figure S1A), confirming that hnRNPA2B1 was sensitive to arsenite stress. Similarly, hnRNPA2B1 was also detected to localize at SGs induced by heat shock, sorbitol, and NaCl (Figures 1A and S1B). Thus, hnRNPA2B1 is a universal SG component associated with SG formation under various stresses.

hnRNPA2B1 harbors two alternative spliced isoforms, A2 and B1, and the shorter isoform (hnRNPA2) lacks 12 amino acids in the N-terminal region and is the main isoform, composing ~90% of the protein in most tissues. To determine which domain of hnRNPA2B1 mediates the association with SGs, we generated different variants and truncated proteins (Figure 1B) and ectopically expressed them in HeLa cells (Figure 1C). The results showed that full-length hnRNPA2, pathogenic mutation hnRNPA2 (D290V), and its C-terminal truncation are mainly located in the nucleus under normal conditions and can translocate onto SGs under arsenite induction (Figure 1C). However, the other three truncated proteins, including N terminus, RNA recognition motif 1 (RRM1), and RRM2, were unable to locate in the nucleus and cannot translocate onto SGs upon arsenite stress but are ubiquitously expressed in the cytoplasm under normal conditions (Figure 1C). Interestingly, the pathogenic mutation hnRNPA2 (D290V) could form G3BP1-positive SGs under normal conditions, indicating its profile of pathogenic protein aggregation (Figure 1C). The C terminus of hnRNPA2B1 is essential for its SG location ability under arsenite stress.

KO of hnRNPA2B1 accelerates the disassembly of arsenite-induced SGs

To test the functional relevance of hnRNPA2B1 for SG metabolism, we generated an hnRNPA2B1 KO HeLa cell line (referred to as hnRNPA2B1 KO) using the CRISPR-Cas9 technique (Figures S1C–S1F) and analyzed the assembly and disassembly of arsenite-induced SGs in hnRNPA2B1 KO cells. The results showed that hnRNPA2B1 depletion does not significantly influence SG assembly compared with WT cell lines under different concentrations of arsenite (Figure 2A), as judged by the quantitative analysis of cells with SGs positive for the SG marker protein G3BP1 (Figure 2B). However, SGs were disassembled notably faster in hnRNPA2B1 KO cells than in WT cells (Figures 2C and 2D). 2.5 h after recovery, only fewer than 10% hnRNPA2B1 KO cells possessed the SGs, whereas 56% WT cells still had SGs (Figure 2D). In addition, hnRNPA2B1 always colocalized with G3BP1-positive SGs during the disassembly process (Figure S1G), indicating its critical role in SG dynamics. These effects were not limited to SGs induced by arsenite stress; indeed, the depletion of hnRNPA2B1 did not influence the SG assembly but specifically led to enhanced SG disassembly under heat shock stress (Figures 2E and 2F). Together, these data indicate that hnRNPA2B1 could retard the disassembly of arsenite-induced SGs during the recovery phase.

Since hnRNPA1 and hnRNPA2B1 are paralogs in the human genome, and both of them are highly expressed in common cell lines and tissues, we next asked whether hnRNPA1 is also involved in SG disassembly. To this end, we first confirmed the association between hnRNPA1 and SGs under four different stresses: arsenite, DTT, sorbitol, and heat shock (Figure S2A), which is consistent with a previous report.[26] We then examined the SG disassembly under arsenite stress by knockdown of hnRNPA1 in WT and hnRNPA2B1 KO cells (Figure S2B). The results showed that the knockdown of hnRNPA1 in WT cells did not influence SG assembly (Figure S2C) but significantly slowed down SG disassembly (Figures S2D and S2E), and the depletion of hnRNPA1 in hnRNPA2B1 KO cells also decelerated SG disassembly (Figures S2D and S2E). These data indicate the convert role of hnRNPA1 and hnRNPA2B1 in regulating SG disassembly.

To test whether the enhanced SG disassembly is reflected by the material property of SG formed in hnRNPA2B1 KO cells, we introduced exogenous GFP-tagged G3BP1 to monitor the mobility of SGs during arsenite stress by fluorescence recovery after photobleaching (FRAP). SGs formed in hnRNPA2B1 KO

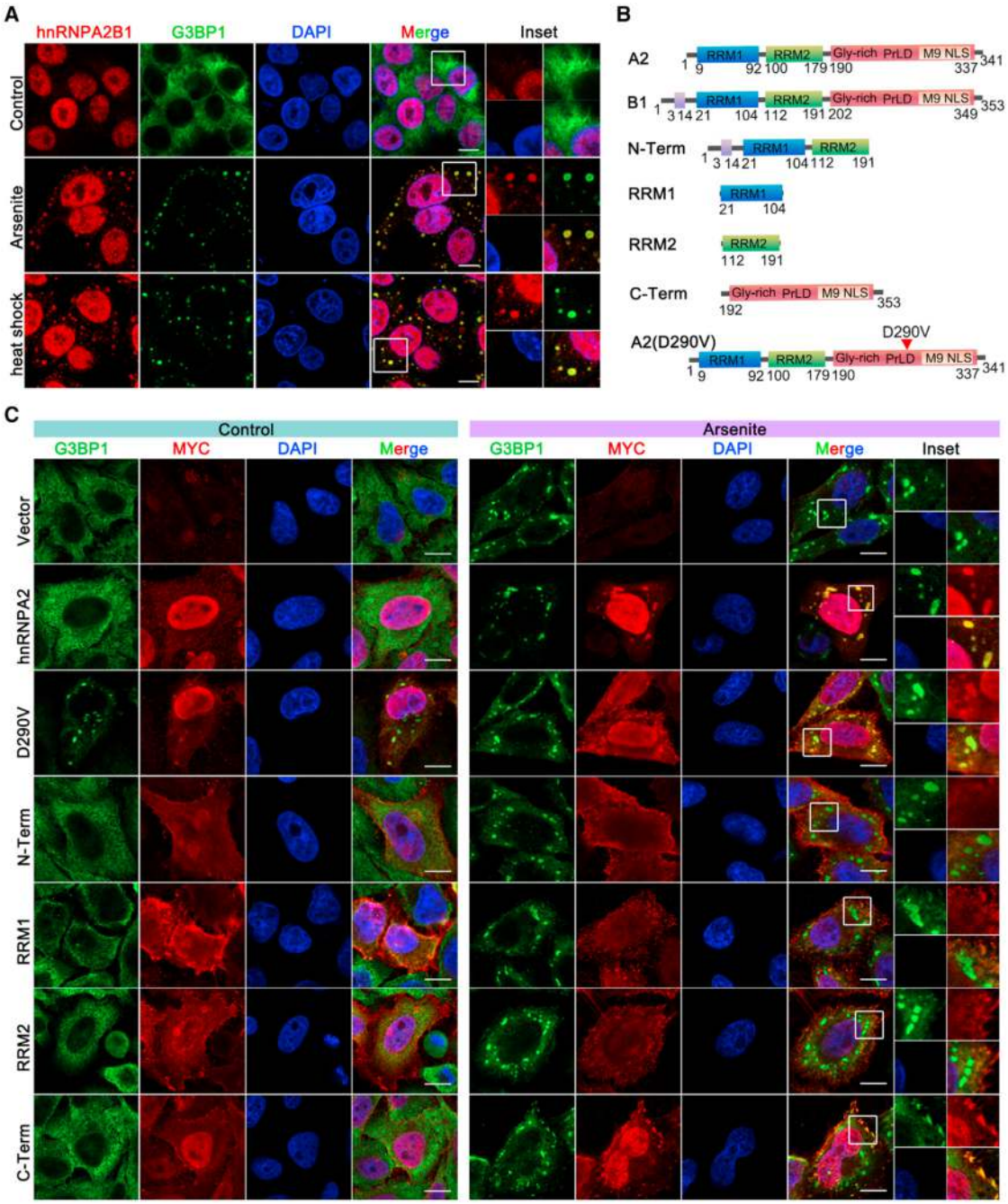

Figure 1. hnRNPA2B1 associates with stress granules (SGs) upon arsenite stress

(A) Immunofluorescence of endogenous hnRNPA2B1 and G3BP1 in HeLa cells subjected to arsenite treatment or heat shock. Scale bars, 10 μm.

(B) Domain architecture of human hnRNPA2B1 and its truncated variants. A2 is the shorter isoform; B1 is the longer isoform. N-Term, N-terminal; RRM, RNA recognition motif; NLS, nuclear localization signal; PrLD, prion-like domain.

(C) Immunofluorescence of MYC (an epitope tagging fused to hnRNPA2B1 and its truncated variants) and G3BP1 in cells transfected with MYC-hnRNPA2B1 variants and treated with arsenite. Scale bars, 10 μm.

cells showed a shorter half-recovery time compared with the WT (Figures 2G and 2H), but the SGs in WT cells had a trend of more recovery near the plateau (Figure 2I), revealing the role of hnRNPA2B1 in defining the motility of arsenite-induced SGs.

Loss of hnRNPA2B1 disturbs the autophagy pathway

Since autophagy has been reported to regulate SG disassembly depending on the initial stressor and SG context,[27,28] we first examined the autophagy level in WT and hnRNPA2B1 KO cells

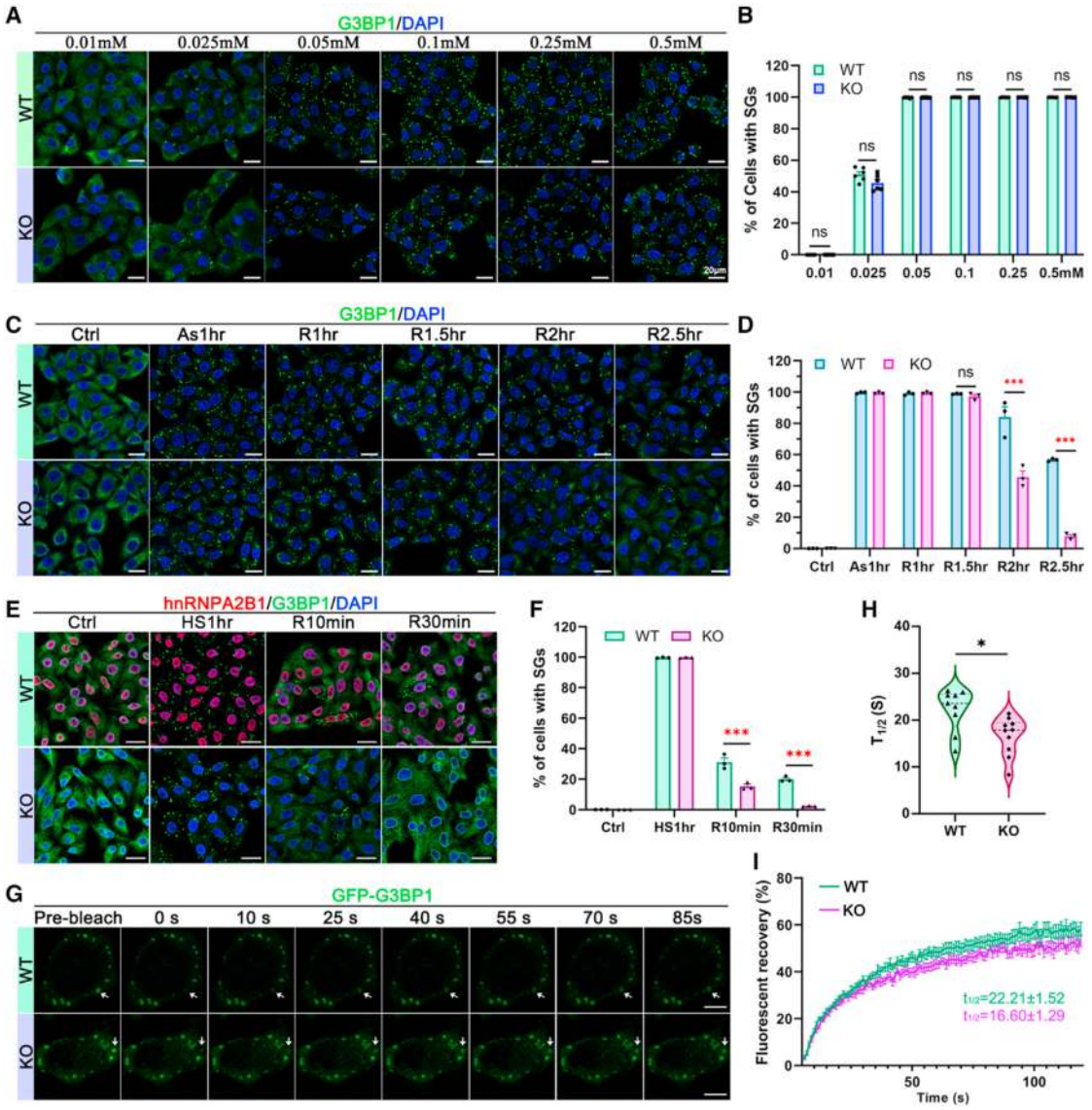

Figure 2. The depletion of hnRNPA2B1 promotes arsenite-induced SG disassembly

(A) Immunofluorescence of G3BP1 in WT and hnRNPA2B1 KO cells exposed to arsenite treatment with different concentrations as indicated for 1 h. Scale bars, 20 μm.

(B) Quantification of cells with SGs in (A). Experiments were performed in triplicate and each time, cells were counted by two different individuals. Over 100 cells were counted per condition.

(C) Immunofluorescence of G3BP1 in WT and hnRNPA2B1 KO cells treated with arsenite and allowed to recover (R) as the indicated time. Scale bars, 20 μm.

(D) Quantification of cells with SGs in (C). Experiments were performed in triplicate.

(E) Immunofluorescence of hnRNPA2B1 and G3BP1 in WT and hnRNPA2B1 KO cells exposed to heat shock and allowed to recover for the indicated time. Scale bars, 20 μm.

(F) Quantification of cells with SGs in (E). Experiments were performed in triplicate. Over 100 cells were counted per condition.

(G) Representative images over time of an FRAP experiment. WT and hnRNPA2B1 KO cells were transfected with GFP-tagged G3BP1 constructs and exposed to arsenite, and then the relative dynamics of SGs were compared by FRAP. Scale bars, 10 μm.

(H) The mean recovery half-time after bleaching.

(I) Average FRAP recovery curves of WT and hnRNPA2B1 KO cells.

Data shown here and in all other quantitations are mean ± SEM unless otherwise specified. ns, not significant. *p < 0.05, **p < 0.01, ***p < 0.001 by two-tailed Student's t test.

to understand the basis underlying the faster SG disassembly upon hnRNPA2B1 deletion. As expected, in hnRNPA2B1 KO cells, the lipidated LC3 (LC3-II) expression level was increased compared with a low level of basal autophagy in WT cells (Figures S3A and S3B), and the increased LC3-II expression levels always occurred under normal conditions, arsenite

treatment, and recovery phase in hnRNPA2B1 KO cells (Figures S3A and S3B). Similarly, the master regulator of the autophagy-lysosome pathway transcription factor EB (TFEB) (Figures S3C and S3D) and the autophagy receptor p62 (Sequestosome-1 [SQSTM1]) (Figure S3E) were also increased in KO cells at all detected time points compared with control cells. Especially during the recovery time after arsenite treatment, TFEB could translocate from the cytoplasm to the nucleus in both WT and KO cells, but the nuclear signals were significantly stronger in KO cells compared with those of WT cells (Figure S3D). However, other detected autophagy-associated proteins showed no apparent change, including ATG7, VCP, and ATG16L (Figure S3A). The simultaneous increase in LC3 and p62 suggests an impaired fusion process of the autophagosome with the lysosome or a dysfunctional autophagic clearance.[29–32] To investigate this, we transfected GFP-mCherry-LC3 plasmid into WT and hnRNPA2B1 KO cells separately to measure the formation of autolysosomes; due to the low pH of the autolysosome, the green fluorescence of the acid-sensitive GFP was quenched upon fusion of the autophagosome with the lysosome, but the red fluorescence of the acid-insensitive mCherry was not lost until the proteins were degraded in the autolysosome.[33] A small number of yellow puncta (mainly indicating autophagosomes) were observed in WT cells; however, yellow puncta were highly accumulated in hnRNPA2B1 KO cells (Figures S3F and S3G), possibly due to a secondary defect in autophagosome maturation and/or lysosome function. Therefore, these results suggest that hnRNPA2B1 may regulate TFEB and p62-related autophagic pathways to control the cell fate.

To investigate whether the abnormally increased protein levels of LC3, TFEB, and p62 are responsible for the more rapid SG disassembly in hnRNPA2B1 KO cells, we knocked down *TFEB* or *p62* in hnRNPA2B1 KO cells (Figures S4A and S4B) and found that the enhanced SG disassembly cannot be blocked by *TFEB* knockdown (Figures S4C and S4D) or *p62* knockdown (Figures S4E and S4F). Subsequently, we used the most widely employed autophagy blocking chemicals, bafilomycin A1 (BafA1) and chloroquine (CQ), to inhibit the last stage of autophagy. BafA1 can increase lysosomal pH and thus inhibit the activity of resident hydrolase and lysosomal degradation capacity.[34–36] CQ mainly impairs the autophagic flux by decreasing autophagosome-lysosome fusion but does not inhibit lysosomal degradation capacity as BafA1 does.[37] The results revealed a successful block of autophagy by adding BafA1 or CQ, showing increased protein levels of LC3-II and p62 (Figure S5A). However, neither BafA1 nor CQ addition could block the fast SG disassembly in hnRNPA2B1 KO cells (Figures S5B–S5D). Thus, hnRNPA2B1 ablation disturbed the autophagy pathway and SGs disassembled independent of autophagy in hnRNPA2B1 KO cells.

The ubiquitination-proteasome pathway is responsible for the faster SG disassembly in hnRNPA2B1 KO cells

Because the ubiquitination-proteasome pathway is required for normal efficient clearance of SGs induced by both arsenite and heat shock,[10,11,38] we sought to determine the effects of the ubiquitination-proteasome pathway in enhanced SG clearance upon hnRNPA2B1 deletion. Accordingly, we tested the impact of several inhibitors of the ubiquitin-proteasome system during SG disassembly in WT and hnRNPA2B1 KO cells, including inhibitors of the 26S proteasome (bortezomib [Btz]), VCP/p97 (CB5083), and UBA1 (TAK243). First, SG clearance was almost completely blocked in both WT (96.15% cells with SG, 475 of 494) and hnRNPA2B1 KO (93.60% cells with SG, 351 of 375) cells upon Btz treatment after recovery for 2 h (Figures 3A and 3B). In addition, after 2.5 h of recovery, the SG disassembly was still firmly blocked in WT cells (89.73% cells with SG, 507 of 565), whereas the block effect was much weaker in hnRNPA2B1 KO cells (56.71% cells with SG, 207 of 365) (Figures 3A and 3B). This result suggests the essential role of proteasome activity in normal SG clearance and hnRNPA2B1-dependent SG disassembly. Second, CB5083 treatment could delay SG disassembly in both WT (96.29% cells with SG, 493 of 512) and hnRNPA2B1 KO cells (68.73% cells with SG, 233 of 339) cells after 2 h of recovery (Figures 3C and 3D). Similar to the Btz treatment, after 2.5 h of recovery, the SG disassembly was still inhibited in WT cells (91.26% cells with SG, 501 of 549), whereas this blocking effect was greatly diminished in hnRNPA2B1 KO cells (35.02% cells with SG, 104 of 297) (Figures 3C and 3D). Therefore, this observation suggests that normal SG disassembly largely depends on VCP activity, but the blockage of VCP activity could only partially inhibit the SG disassembly upon hnRNPA2B1 depletion. Third, in the case of TAK243 treatment, about 70.99% (372 of 524) of WT cells contained SGs, whereas only 49.19% (114/232) of hnRNPA2B1 KO cells had SGs after 2 h of recovery (Figure 3E). Moreover, after 2.5 h of recovery, ~38.63% (192 of 496) of WT cells still harbored SGs, whereas ~23.33% (77 of 330) of hnRNPA2B1 KO cells contained SGs (Figure 3E), which indicates that the blockage effect of TAK243 on SG disassembly would weaken upon hnRNPA2B1 ablation. Together, these data showed that the inhibition effect of Btz was the most efficient one among the detected three inhibitors, and its inhibition effect was comparable between WT and hnRNPA2B1 KO cells. However, the inhibition effect of SG disassembly of CB5083 and TAK243 was much weaker in hnRNPA2B1 KO cells than in WT cells.

These results raised two possible explanations, with the first being that the conventional pathways for SG disassembly discovered so far became much stronger upon hnRNPA2B1 KO; the other might be that some unknown pathways responsible for SG disassembly were activated in hnRNPA2B1 KO cells. To test the first possibility, we increased the concentration of the three inhibitors by 2-fold. The blockage effects of a doubled concentration of the three inhibitors in hnRNPA2B1 KO cells could nearly achieve that of WT cells treated with normal concentrations (Figures 3E–3G), except that doubled CB5083 in hnRNPA2B1 KO cells still could not achieve the blocking efficiency in WT cells after 2.5 h of recovery (Figure 3G). Altogether, our findings indicate that the ubiquitination-proteasome pathway is essential for SG disassembly in both WT and hnRNPA2B1 KO cells and is responsible for the faster SG disassembly in hnRNPA2B1 KO cells.

hnRNPA2B1 interacts with G3BP1 to regulate SG disassembly mediated by G3BP1-USP10/Caprin-1 interaction and G3BP1 ubiquitination

To gain more insight into the mechanisms underlying the enhanced SG disassembly in hnRNPA2B1 KO cells, we next

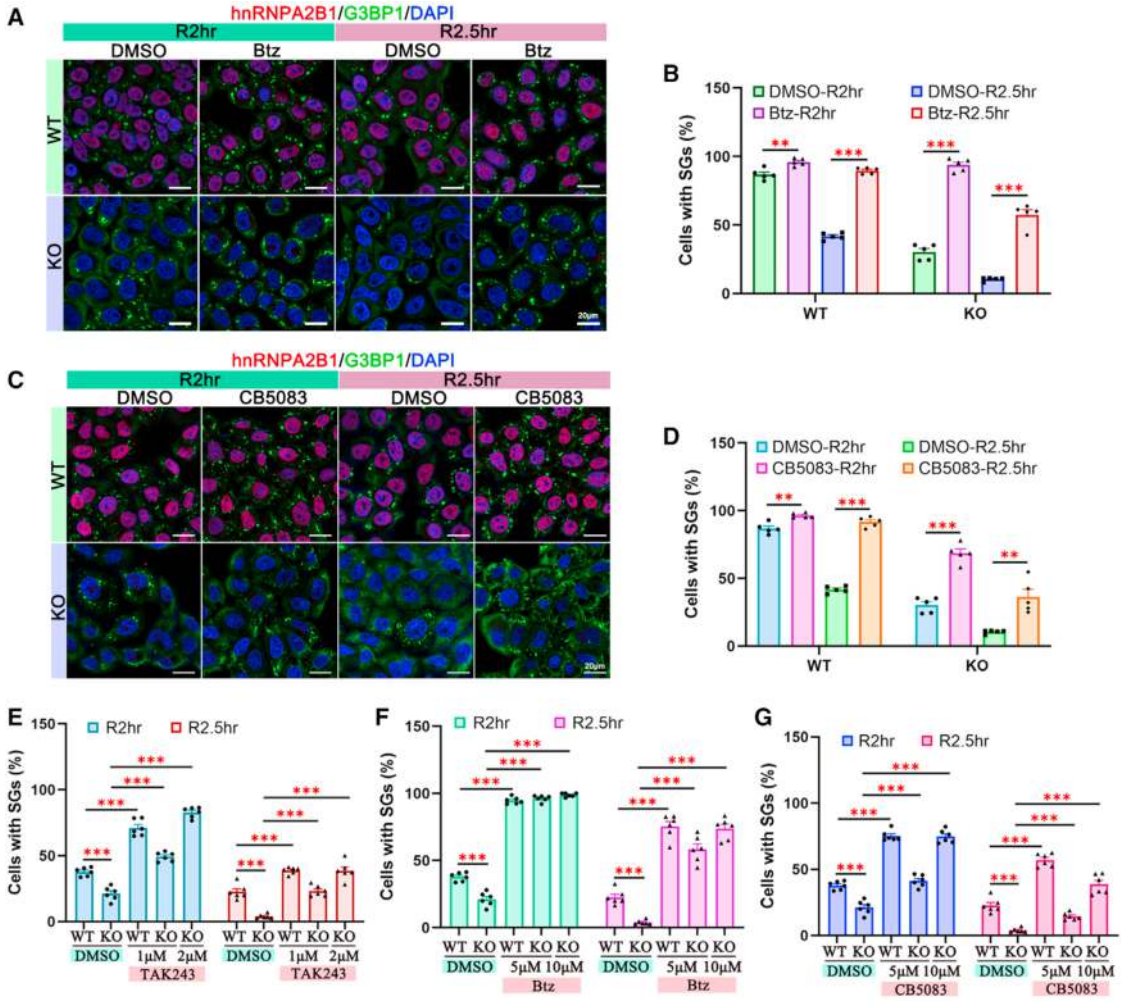

Figure 3. Blockage of the ubiquitination-proteasome pathway inhibits the faster SG disassembly in hnRNPA2B1 KO cells

(A) Immunofluorescence of hnRNPA2B1 and G3BP1 after treatment with the indicated chemicals (DMSO or bortezomib [Btz]) and recovery for 2 h (R2hr) and 2.5 h (R2.5hr), respectively. Scale bars, 20 μm.

(B) Quantification of cells with SGs in (A). Experiments were repeated five times. Over 100 cells were counted per condition.

(C) Immunofluorescence of hnRNPA2B1 and G3BP1 in cells treated with DMSO or CB5083 and recovered for 2 h (R2hr) and 2.5 h (R2.5hr), respectively. Scale bars, 20 μm.

(D) Quantification of cells with SGs in (C). Experiments were repeated five times. Over 100 cells were counted per condition.

(E–G) Quantification of cells with SGs after treatment with TAK243 (E), Btz (F), and CB5083 (G) at R2hr and R2.5hr. Experiments were performed in triplicate, and each time cells were counted by two different individuals. Over 100 cells were counted per condition.

All data are shown as mean ± SEM. *p < 0.05, **p < 0.01, ***p < 0.001 by two-tailed Student's t test.

immunoprecipitated endogenous hnRNPA2B1 by using WT HeLa cell extracts and performed mass spectrometry to generate a list of hnRNPA2B1-interacting proteins (jPOST: JPST002463). In total, we identified 878 proteins that are highly involved in multiple aspects of RNA processing, including metabolism of RNA, translation, ribonucleoprotein complex biogenesis, RNA localization and stabilization, and SG assembly (Figure S6A). Notably, 18 core SG proteins, 16 pre-stress seed proteins (4 proteins are engaged in spermatogenesis), and 29 disassembly-engaged proteins (DEPs) were found among hnRNPA2B1-interacting proteins (Figure 4A). We thus used hnRNPA2B1 and its 35 interacting proteins involved in SG assembly or core SG proteins and pre-stress proteins to construct a protein interaction network (Figure S6B). Next, immunoprecipitation results showed that, except for SFPQ, the other six selected proteins interacted with hnRNPA2B1 under normal conditions, and three proteins (G3BP1, NONO, and TDP43) interacted with hnRNPA2B1 no matter whether arsenite was present, but the interactions between hnRNPA2B1 and the other three proteins (PABPC1, FXR1, and FMR1) became too weak and were barely detectable after arsenite addition (Figures 4B and S6C). Furthermore, the G3BP1-interacting proteins (G3BP2, Caprin-1, and USP10) and ZFAND1 (a protein that promotes arsenite-induced SGs by recruiting VCP and the 26S proteasome[39]) were also confirmed to interact with hnRNPA2B1 (Figures 4C and 4D), and the interactions between hnRNPA2B1

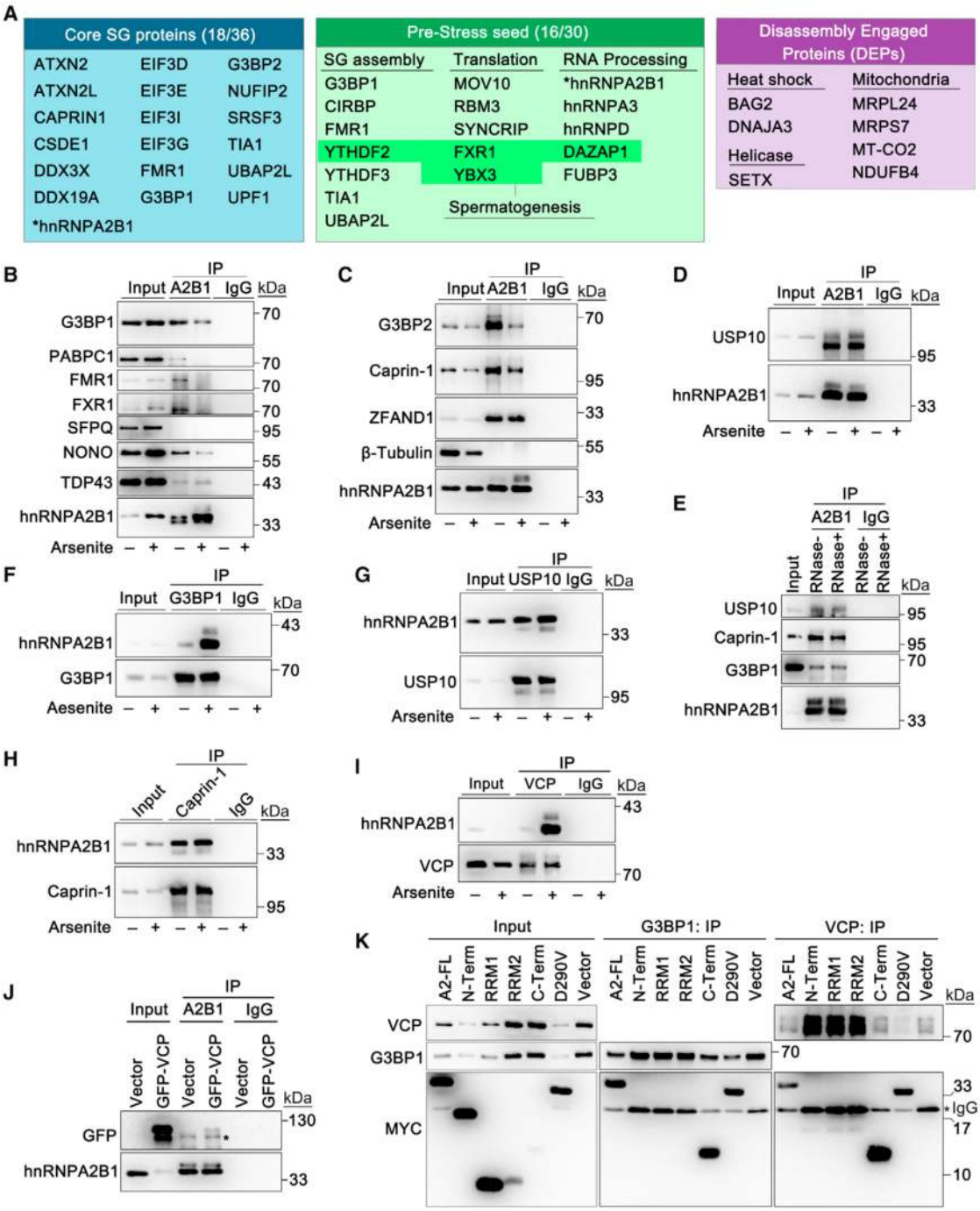

Figure 4. hnRNPA2B1 interacts with several core SG component proteins

(A) Selected hnRNPA2B1-interacting proteins included in core SG, pre-stress seed, and disassembly-engaged proteins (DEPs). hnRNPA2B1 itself (asterisk) is also contained in core SG and pre-stress seed proteins.

(B–D) Co-immunoprecipitation (coIP) assay showing the interaction protein of hnRNPA2B1 under the normal condition or arsenite treatment.

(E) CoIP using an hnRNPA2B1 antibody in arsenite-treated cells incubated with RNaseA or left untreated.

(F–I) Reciprocal IP using antibodies of G3BP1 (F), USP10 (G), Caprin-1 (H), and VCP (I) in cells under normal conditions or arsenite treatment. Input and IP samples were immunoblotted for the indicative antibodies.

(J) Lysates of cells ectopically expressing GFP-tagged VCP or empty vector were subjected to hnRNPA2B1 IP and immunoblotted for GFP and hnRNPA2B1. An asterisk indicates a non-specific band.

(K) Lysates of cells ectopically expressing MYC-tagged hnRNPA2 full-length (A2-FL), hnRNPA2 variants corresponding to Figure 1B, hnRNPA2-D290V, or empty vector were subjected to G3BP1 IP or VCP IP.

and G3BP1/USP10/Caprin-1 were RNA independent (Figure 4E). Of note, the key SG component proteins, including Caprin-1, FMR1, FXR1, and USP10, were retrieved faster from SGs in hnRNPA2B1 KO cells than that of WT during the recovery phase, which is akin to G3BP1 (Figures S6D and S6E).

To further investigate the molecular links between hnRNPA2B1 and core SG proteins (G3BP1/USP10/Caprin-1) and the ubiquitination-associated protein VCP, we carried out the reciprocally immunoprecipitated assays using G3BP1, USP10, Caprin-1, and VCP antibodies and further confirmed their interactions with hnRNPA2B1 under normal and arsenite treatment conditions (Figures 4F–4I). In addition, we ectopically overexpressed GFP-VCP in HeLa cells and performed an immunoprecipitation experiment using the hnRNPA2B1 antibody, confirming the interaction of VCP and hnRNPA2B1 (Figure 4J). Further immunoprecipitation experiments by ectopically overexpressed WT and truncated hnRNPA2B1 variants showed that both G3BP1 and VCP could bind specifically with the C-terminal domain of hnRNPA2B1 (Figure 4K). Since the pathogenic mutation hnRNPA2 (D290V) is located in the C-terminal domain, we asked whether the mutation alters the interaction between hnRNPA2B1 and G3BP1. MYC-tagged WT hnRNPA2 and its mutant D290V were transfected into HeLa cells, and immunoprecipitation with G3BP1 or MYC antibodies, respectively, showed that the hnRNPA2B1-G3BP1 interaction is not affected by the D290V mutation (Figure S6F). Since VCP could utilize different cofactors, such as ZFAND1 under arsenite stress and FAF2 under heat shock, to participate in SG disassembly,[10] we asked whether the colocalization intensity of VCP with SGs is affected upon hnRNPA2B1 depletion. Interestingly, we found that VCP could colocalize with SGs but did not show any noticeable intensity change between WT and hnRNPA2B1 KO cells under arsenite treatment and recovery duration (Figure S6G). Moreover, the interactions of VCP-ZFAND1, VCP-FAF2, VCP-G3BP1, G3BP1-ZFAND1, and G3BP1-FAF2 displayed no apparent changes between WT and hnRNPA2B1 KO cells under arsenite treatment (Figures S6H and S6I). Therefore, hnRNPA2B1 interacts with G3BP1 and VCP via its C-terminal domain, but the interaction of hnRNPA2B1-VCP may not be responsible for regulating SG disassembly under arsenite stress.

We next focused most of our subsequent investigations on the interaction of hnRNPA2B1-G3BP1 through analyzing the interaction strength between G3BP1 and its key interacting proteins. Under the normal condition, the interactions between G3BP1 and its key interacting proteins showed no noticeable change, including Caprin-1, USP10, G3BP2, and PABPC1 (Figure 5A, left). Interestingly, the interactions of G3BP1-USP10 and G3BP1-Caprin-1 were significantly weaker in hnRNPA2B1 KO cells compared with WT cells under arsenite treatment, whereas interactions of G3BP1-G3BP2 and G3BP1-PABPC1 showed no apparent changes (Figure 5A, center). Notably, all four detected proteins exhibited weaker interaction with G3BP1 after recovery for 1.5 h (Figure 5A, right). Furthermore, we observed increased G3BP1 ubiquitination upon arsenite treatment for 1 h (1.36 in KO vs. 1.00 in WT cells) and after recovery for 1.5 h (1.24 in KO vs. 1.00 in WT cells) in hnRNPA2B1 KO cells compared with WT cells, (Figure 5B, top). Next, to further determine which types of polyubiquitin chains mainly contribute to the increased total G3BP1 ubiquitination, we detected the endogenous levels of K48- and K63-linked chains, which are the most abundant and well-characterized linkage types.[40] The levels of K48-linked polyubiquitination of G3BP1 showed a slight increase (1.26 in KO vs. 1.00 in WT cells) (Figure 5B, center), whereas the K63-linked ubiquitination of G3BP1 exhibited a much higher level upon arsenite treatment (1.40 in KO vs. 1.00 in WT cells) (Figure 5B, bottom). On the contrary, no obvious change was observed under heat shock stress, including total G3BP1 ubiquitination and the endogenous K48- and K63-linked chains (Figure 5C). Taken together, these data suggest that hnRNPA2B1 mediates the interplay of G3BP1-USP10 and/or G3BP1-Caprin-1, thereby regulating SG disassembly via G3BP1 ubiquitination under arsenite stress.

USP10 stabilizes and deubiquitinates G3BP1

Since USP10 is a ubiquitin-specific protease, and we observed the decreased G3BP1-USP10 interaction and the increased ubiquitination level of G3BP1 in hnRNPA2B1 KO cells, subsequently, we mainly focused on the mechanism of G3BP1 and its partner USP10 in SG disassembly and asked whether USP10 might function to deubiquitinate G3BP1. First, we observed that the knockdown of USP10 decreased G3BP1 protein levels, and two different small interfering RNAs (siRNAs) targeting *USP10* behaved similarly (Figure 5D); in parallel, ectopic overexpression of GFP-tagged USP10 resulted in G3BP1 elevation in a dose-dependent manner (Figure 5E). Furthermore, the endogenous protein level of G3BP1 showed no obvious changes in the four detected conditions (control [Ctrl], arsenite treatment for 1 h [As1h], recovery for 1.5 h [R1.5h], and recovery for 2 h [R2h]) (Figure S6J). We next investigated whether USP10 regulates the level of G3BP1 ubiquitination, using the proteasome inhibitor MG132 to observe G3BP1 ubiquitination in Figure 5F. USP10 knockdown significantly increased the total ubiquitination levels and G3BP1 ubiquitination (3.83 in si*USP10* vs. 1.00 in siNC). In contrast, the ectopic expression of GFP-tagged USP10 significantly decreased the total ubiquitination level and G3BP1 ubiquitination (0.24 in GFP-USP10 vs. 1.00 in vector) (Figure 5F). These results indicate that G3BP1 is a substrate of USP10 and that USP10 regulates G3BP1 ubiquitination.

hnRNPA2B1 depletion promotes the disassembly of SGs containing ALS-associated mutated FUS protein

A range of genes encoding RBPs that function in the SG reaction bear pathological mutations that are prone to accumulate within SGs, such as ATXN2, FUS, hnRNPA0, hnRNPA1, hnRNPA2B1, and TDP43, as summarized by Wolozin and Ivanov.[8] To detect whether hnRNPA2B1 deletion can enhance the disassembly of a pathological mutation protein, the FUS-R521C mutation was selected, as it is a frequent and highly penetrant amyotrophic lateral sclerosis (ALS)-associated mutation, and it has been found in both familial and sporadic ALS patients in a geographically unrelated manner with high disease penetrance.[41–46] We transfected plasmids encoding WT FUS (FUS^{WT}) or its R521C mutant (FUS^{R521C}) protein into WT and hnRNPA2B1 KO cells, respectively, and the transfected plasmid amount was controlled to ensure that the ectopically overexpressed FUS^{WT} and FUS^{R521C} themselves could not induce SGs in WT and hnRNPA2B1 KO cells under basal conditions (Figures 6A and

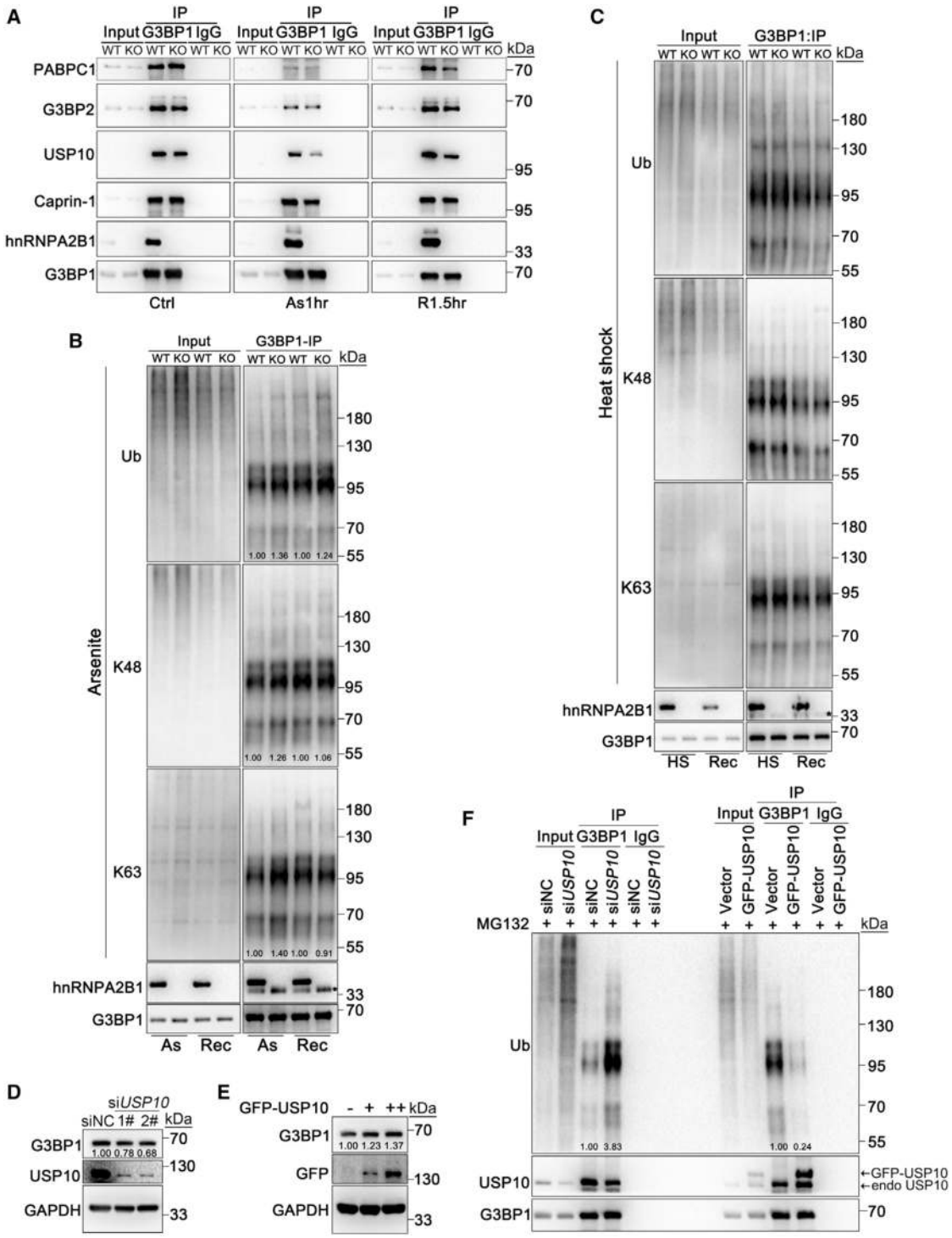

Figure 5. hnRNPA2B1 regulates the G3BP1-USP10 interaction strength and G3BP1 ubiquitination level under arsenite stress

(A) CoIP assay showing the attenuated association of G3BP1-USP10 and G3BP1-Caprin-1 under arsenite treatment (As1hr). Ctrl, normal condition.

(B and C) IP assay showing the endogenous ubiquitination and K48- or K63-linked polyubiquitination levels of G3BP1 under arsenite treatment (B) and heat shock (C). As in (B) means arsenite treartment for 1 h; HS in (C) means heat shock for 1 h; Rec, recovery for 1.5 h in (B) and 30 min in (C). Ubiquitination levels (normalized by G3BP1 levels) were quantified. The asterisk indicates an immunoglobulin G (IgG) band.

(D and E) Immunoblot showing the effect of *USP10* knockdown by using two independent siRNAs (D) or overexpression by increasing amounts of GFP-tagged USP10 (E) on the level of G3BP1. G3BP1 levels (normalized by GAPDH levels) were quantified. NC, negtive control.

(F) Immunoblot showing G3BP1 ubiquitination levels *in vivo* regulated by USP10 knockdown (left) or overexpression (right). Cells were treated with MG132 (10 μM) 4 h before harvest. Ubiquitination levels (normalized by G3BP1 levels) were quantified.

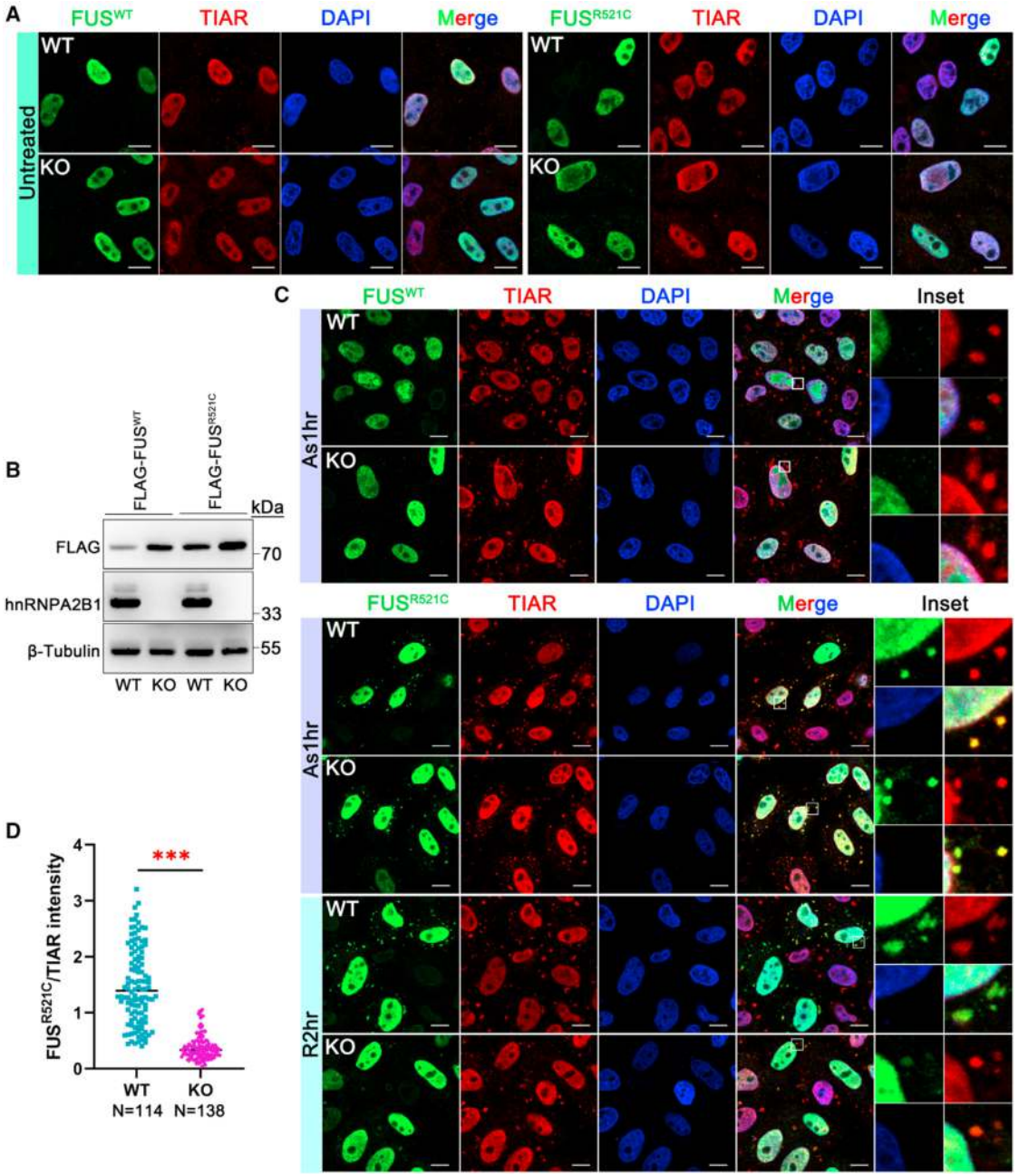

Figure 6. The pathological FUS mutant (R521C) disassembles faster from SGs in hnRNPA2B1 KO cells

(A) WT and hnRNPA2B1 KO cells under normal conditions were transfected with plasmids encoding FLAG-tagged wild-type FUS (FUS^{WT}) and FUS-R521C (FUS^{R521C}) and stained for FLAG and TIAR (a SG marker protein). Scale bars, 10 μm.

(B) Immunoblot showing the ectopic expression of transfected FLAG-FUS^{WT} or FLAG-FUS^{R521C} in (B).

(C) Immunofluorescence of FLAG and TIAR in cells, transfected with FLAG-FUS^{WT} or FLAG-FUS^{R521C}, treated with arsenite (As1hr), and recovered for 2 h (R2hr). Scale bars, 10 μm.

(D) Quantification of the intensity ratio of FUS^{R521C}/TIAR on SGs at R2hr. Over 100 SGs were counted for each group. Data are shown as mean ± SEM. ***$p < 0.001$ by two-tailed Student's t test.

6B). Subsequently, after arsenite treatment, FUS^{R521C} translocated onto SGs in the majority of FUS^{R521C}-positive cells, whereas FUS^{WT} was rarely seen in SGs in both WT and hnRNPA2B1 KO cells (Figure 6C, top and center), which was in agreement with previous results from cultured primary motor neurons from WT and FUS^{R521C} knockin homozygous mutant spinal cords.[47] To study the disassembly of FUS^{R521C} from SGs, we analyzed the intensity change of FUS^{R521C} on SGs

during recovery. In WT cells, FUS^{R521C} was still strongly colocalized in the remaining SGs after R2H (Figure 6C). However, the intensity of FUS^{R521C} on the remaining SGs was strikingly decreased in hnRNPA2B1 KO cells compared with that in WT cells (Figures 6C, bottom, and 6D). Together, these results indicate that ALS-causing FUS mutations were disassembled faster from SGs upon hnRNPA2B1 depletion, revealing a highly conserved role of hnRNPA2B1 in eliminating physiological and pathological SGs.

Ablation of hnRNPA2B1 in mice causes SCOS and leads to faster SG disassembly in Sertoli cells

To explore the physiological role of hnRNPA2B1 *in vivo*, we first detected the expression pattern of hnRNPA2B1 in multiple mouse tissues. Both mRNA and protein of hnRNPA2B1 were ubiquitously expressed in all detected tissues, but with the highest protein expression level in the testes and heart (Figures S7A and S7B), and expressed from post-natal day 0 (P0) to adult in the testes, with hnRNPA2 as the main isoform (Figures S7C and S7D). hnRNPA2B1 was ubiquitously expressed in the nucleus of Sertoli cells, mitotic spermatogonia, meiotic spermatocytes, and haploid round spermatids and almost undetectable in elongating spermatids (Figure S7E). Immunofluorescence staining of hnRNPA2B1 with WT1 (a Sertoli cell marker) in the developing testes (P1, P7, P14, P21, P26, P35, and P42) further revealed that hnRNPA2B1 is extensively expressed in Sertoli cells and germ cells, including prospermatogonia (P1) and spermatogonia (P7), and highly expressed in pachytene spermatocyte and round spermatids (P14–P42) (Figure S7F). Together, hnRNPA2B1 is highly expressed in Sertoli cells, meiotic spermatocytes, and post-meiotic round spermatids (RS) and may play an essential role in male germ cell development.

We next established a *Hnrnpa2b1* gene global KO mouse model and found that the KO mice (referred as *Hnrnpa2b1* KO) could survive normally with no obvious developmental defects. However, the *Hnrnpa2b1* KO adult males were completely infertile and produced no pups when co-caged with fertility-proven WT females. Since the function of hnRNPA2B1 had been reported in other systems using conditional KO mice, such as the immune system,[23] we mainly focused on its role in spermatogenesis in this study. Gross histological analyses of testes showed smaller testis size and decreased testis/body weight from P14 onward in *Hnrnpa2b1* KO mice compared with WT Ctrls (Figures 7A and 7B). Western blot and immunofluorescence assays confirmed the successful deletion of hnRNPA2B1 in mouse testes (Figures 7C and 7D). Inspiringly, in adult *Hnrnpa2b1* KO mice (P45), the germ cells were massively lost, leaving only somatic cells that resembled the SCOS associated with human infertility (Figures 7D and 7E). To ascertain the stage at which defects in spermatogenesis occurred, we performed histology and immunofluorescence analyses and found that mouse *Hnrnpa2b1* KO seminiferous tubules had germ cell numbers at P1 comparable with WT Ctrls (Figures 7F and S7G). However, germ cells started to decline at P2, then underwent obvious loss from P3, and were either wholly depleted or significantly reduced in *Hnrnpa2b1* KO seminiferous tubules at P7 (Figures 7F and S7G). Co-staining of TRA98 (also called GCNA1, a germ cell marker) and WT1 at P7 and P14 further confirmed the phenotype of SCOS of male *Hnrnpa2b1* KO mice (Figure S7H). Thus, these data indicate that hnRNPA2B1 is essential for spermatogenesis and male fertility.

In males, arsenic poisoning significantly affects fertility,[48,49] and Sertoli cells have been identified as one of the principal targets of heavy metals, including arsenic.[50] To further determine the function of hnRNPA2B1 in SG disassembly, we first isolated Sertoli cells from P8–P10 WT and *Hnrnpa2b1* KO mouse testes and confirmed its high purification (above 80%) by staining with WT1 (Figure S7I). Co-staining hnRNPA2B1 and G3BP1 confirmed the deletion and primary nucleus localization of hnRNPA2B1 in Sertoli cells (Figure 7G). hnRNPA2B1 could also translocate onto SGs after arsenite treatment (Figure 7H), and the SGs in mouse *Hnrnpa2b1* KO Sertoli cells disassembled exceptionally faster than WT Ctrls after R1.5h (Figures 7I and 7J), which was similar to that in HeLa cells. hnRNPA2B1 deletion could speed up the arsenite-induced SG disassembly in both human HeLa and mouse Sertoli cells, indicating its conserved function in maintaining SG homeostasis.

DISCUSSION

Different from the functions of the previously reported proteins whose depletion or activity inhibition usually led to SG accumulation, such as ZFAND1,[39] ULK1/ULK2,[51] VCP,[27] HSP70,[52] and HSP90,[53] we identified hnRNPA2B1 as a critical regulator of arsenite-induced SG turnover and were surprised to find that the KO of hnRNPA2B1 accelerates the disassembly of arsenite-induced SGs primarily depending on the ubiquitin-proteasome system but not the autophagy pathway. These data are consistent with the theory that the majority of SGs are short lived and highly dynamic and disassemble rapidly in the recovery phase, whereas only a minor fraction of SGs that are less dynamic or SGs induced by prolonged stress or disease mutations are prone to be targeted by autophagy for clearance.[10,52,53] Although hnRNPA1 and hnRNPA2B1 showed high similarity in their protein structures, hnRNPA1 is not present in pre-stress seed[54] and plays a different role in SG disassembly with hnRNPA2B1, which might be caused by the differences of post-translational modifications or protein-protein interaction between hnRNPA1 and hnRNPA2B1 during SG dynamics.

SGs are gradually disassembled in WT cells during the recovery period, whereas they are suddenly decreased by about 50% in half an hour. Considering that SGs are formed when the sum of protein-protein, protein-RNA, and RNA-RNA interactions crosses the percolation threshold and are disassembled when the interaction network falls below the percolation threshold, our findings provided the compelling hypothesis that hnRNPA2B1 can regulate the speed of reaching the disassembly percolation threshold of LLPS by interacting with G3BP1; when the threshold is bypassed, SGs probably become highly unstable and disassemble more rapidly due to weaker protein interaction and a higher ubiquitination level of G3BP1 in the absence of hnRNPA2B1. In addition, we also found that hnRNPA2B1 could interact with 29 DEPs, which included 202 proteins more enriched during the disassembly process than under arsenite stress,[54] thereby raising another possibility: that hnRNPA2B1 forms a protein complex with DEPs to be involved in SG disassembly.

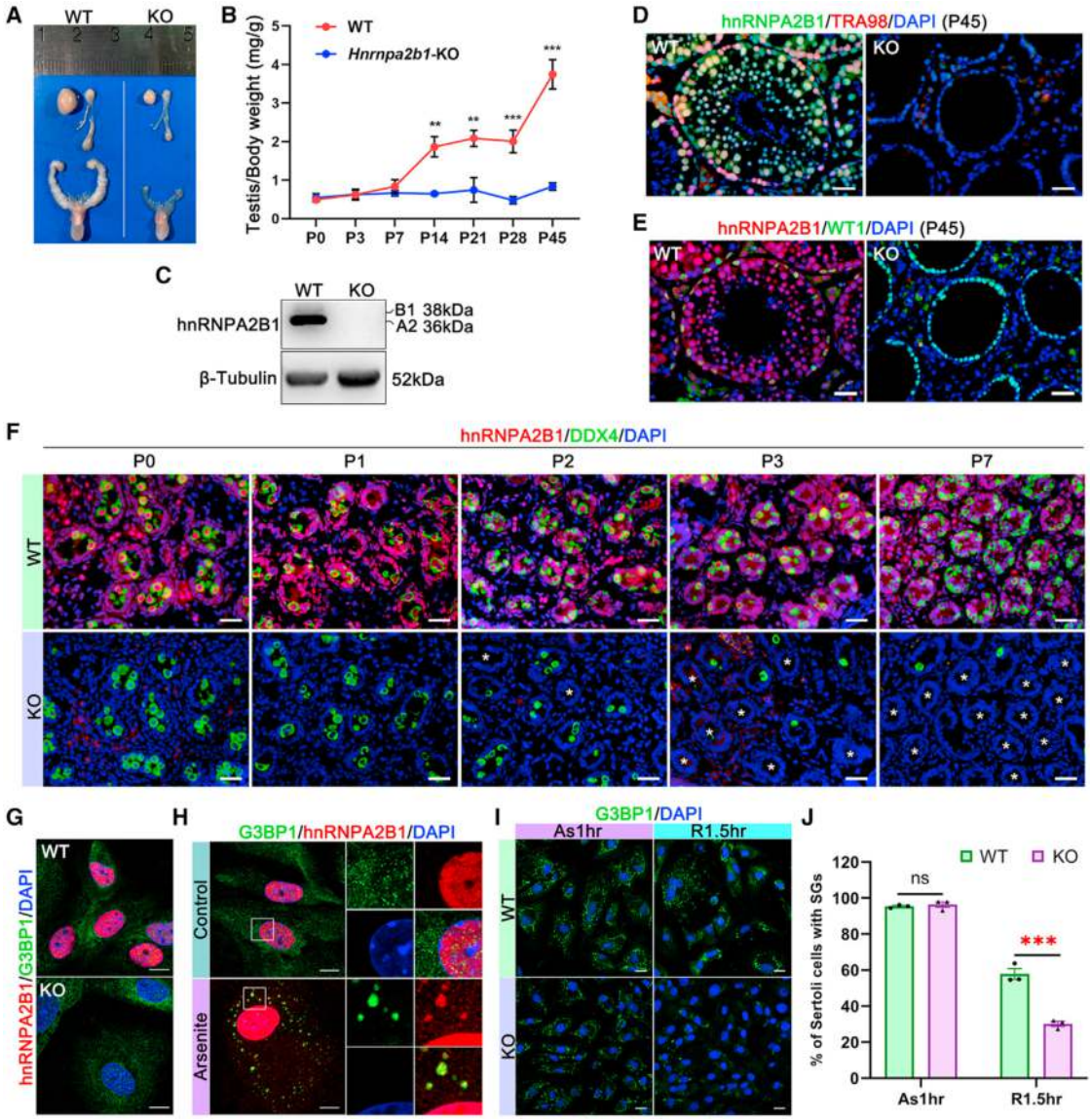

Figure 7. Male *Hnrnpa2b1* KO mice are infertile, and SGs disassemble faster in mouse *Hnrnpa2b1* KO Sertoli cells

(A) The gross morphology of the testes, epididymis, and seminal vesicles from adult WT and *Hnrnpa2b1* KO mice.

(B) Testis growth curve showing that *Hnrnpa2b1* KO testes were significantly decreased from P14.

(C) Immunoblot showing the hnRNPA2B1 protein level in adult WT and *Hnrnpa2b1* KO testes.

(D and E) Immunofluorescence of hnRNPA2B1 and TRA98 (D) and WT1 (E) on WT and *Hnrnpa2b1* KO testicular sections. Scale bars, 50 μm.

(F) Immunofluorescence of hnRNPA2B1 and DDX4 on testicular sections from WT and *Hnrnpa2b1* KO mice at P0, P1, P2, P3, and P7. White asterisks indicate agametic tubules. Scale bars, 50 μm.

(G) Immunofluorescence of hnRNPA2B1 and G3BP1 in the purified Sertoli cells from P8–P10 WT and *Hnrnpa2b1* KO testes. Scale bars, 10 μm.

(H) Immunofluorescence of hnRNPA2B1 and G3BP1 in purified Sertoli cells treated with arsenite. Scale bars, 10 μm.

(I) Immunofluorescence of G3BP1 in purified Sertoli cells, which were treated with arsenite (As1hr) and recovered for 1.5 h (R1.5hr). Scale bars, 10 μm.

(J) Quantification of cells with SGs in (I). Experiments were performed in triplicate.

All data are shown as mean ± SEM. ns, not significant. *p < 0.05, **p < 0.01, ***p < 0.001 by two-tailed Student's t test.

G3BP1 interacts with many proteins; some of them are SG nucleators (Caprin1[55]) and/or core SG components,[3] and several of them have been proven to be involved in SG assembly, such as Caprin1, USP10,[56] and HDAC6.[57] However, there is much less research on the molecular mechanism of G3BP1-interacting proteins in regulating SG disassembly than SG assembly; the autophagy-inducing kinase ULK1 interacts with several SG proteins (G3BP1, USP10, and Caprin1), and ULK1/2 regulates the SG disassembly independent of the canonical components of the autophagy machinery but via phosphorylation and activation the ATPase VCP.[51] Another G3BP1-interacting protein, glycyl-tRNA synthetase (GlyRS), is

translocated to SGs upon stress, where the CMT2 (Charcot-Marie-Tooth type 2 neuropathy)-causing mutant GlyRS acquires aberrantly increased binding to G3BP1, leading to a perturbed G3BP1-centric core SG network and increased stress vulnerability of motor functions,[58] suggesting an SG-mediated interplay between disease-causing genes and environmental stress.

Emerging evidence has highlighted impaired SG dynamics as a primary driver of cancer[59] and neurodegeneration, particularly in ALS and frontotemporal dementia (FTD),[8,60] where mutant TDP43, FUS, C9orf72, or other pathological proteins form insoluble protein aggregates in SGs, thus disturbing LLPS-dependent SG dynamics.[61–64] Therefore, managing SG dynamics is a promising field to develop potential therapeutic strategies by targeting SG proteins in related disorders. We found that ALS-causing FUS^{R521C} was disassembled faster from SGs in hnRNPA2B1 KO cells. Together with the recent finding that NEDP1 inhibition could ameliorate ALS phenotypes via promoting SG disassembly in *C. elegans*,[40] it may provide a reward to silence hnRNPA2B1 as a potential way to inhibit the pathological progress or enhance SG clearance in related diseases.

Importantly, the faster SG disassembly in hnRNPA2B1 KO HeLa cells was phenocopied by purified Sertoli cells from *Hnrnpa2b1* KO mice, indicating the conserved function and regulatory pathway by hnRNPA2B1 *in vitro* and *in vivo*, raising the hypothesis that hnRNPA2B1 is critical in maintaining SG homeostasis of Sertoli cells to regulate spermatogenesis and male fertility under arsenic exposure. Similar but with a reverse function as this study, our recent work reported that RNA-binding protein SERBP1 could promote SG disassembly in both arsenite or heat shock induction and is essential for protecting male germ cells from thermostimulus damage.[65] Therefore, more molecular insights into SG disassembly are needed in the future.

In summary, our data uncover a conserved role of hnRNPA2B1 in human HeLa cells and mouse Sertoli cells that interacts with G3BP1 to modulate the interplay of G3BP1-USP10 and/or G3BP1-Caprin-1, thereby repressing SG disassembly via ubiquitination of G3BP1 mediation, and reveal a critical function in spermatogenesis and male fertility. These findings may give insights into the pathogenesis of arsenite stress-induced diseases, including male fertility.

Limitations of the study

To investigate the reason for decreased interaction between hnRNPA2B1 and its interaction proteins after arsenite treatment, we performed immunoprecipitation using different hnRNPA2B1 antibodies (sc-374053 from Santa Cruz Biotechnology and 14813-1-AP from Proteintech) and using an MYC antibody after ectopic overexpression of MYC-tagged hnRNPA2 (Figure S6C), but the results were always the same. Coincidentally, this phenomenon was also observed in the UBAP2L immunoprecipitation (a high-affinity binding partner of G3BP1).[4] Therefore, resolving this question will require more consideration, including but not limited to the modification of hnRNPA2B1 and/or its interaction partners or the different interaction contributions from the nucleus and cytoplasm.

At present, we are mainly focusing on the G3BP1-USP10 interaction but not the G3BP1-Caprin-1 association; it is still unclear how hnRNPA2B1 regulates the G3BP1-USP10-Caprin-1 complex to affect SG disassembly. Furthermore, except for ubiquitination, whether other factors regulate the faster SG disassembly upon hnRNPA2B1 deletion remains unknown, as recent studies point to heat shock proteins and RNA helicases as key regulators.[54] Notably, G3BP1 ubiquitination behaves differently under arsenite and heat shock stress. Therefore, further investigations are needed to elucidate the mechanisms of hnRNPA2B1 in SG disassembly under arsenite and heat shock.

STAR★METHODS

Detailed methods are provided in the online version of this paper and include the following:

- KEY RESOURCES TABLE
- RESOURCE AVAILABILITY
  - Lead contact
  - Materials availability
  - Data and code availability
- EXPERIMENTAL MODEL AND STUDY PARTICIPANT DETAILS
  - Generation of *Hnrnpa2b1* gene knockout mice
  - *hnRNPA2B1* knockout HeLa cell line generation
  - Mice
- METHOD DETAILS
  - Plasmids and siRNA construction
  - Cell culture and transfection
  - Arsenite treatment, heat shock and drug treatments
  - Immunoprecipitation
  - Mass spectrometry
  - Western blotting
  - Immunofluorescence of cells
  - Histological analysis and immunostaining of testis
  - Sertoli cell purification
  - Fluorescence recovery after photo bleaching
- QUANTIFICATION AND STATISTICAL ANALYSIS

SUPPLEMENTAL INFORMATION

Supplemental information can be found online at https://doi.org/10.1016/j.celrep.2024.113769.

ACKNOWLEDGMENTS

We thank Dr. Juanjuan Gong (Beijing Children's Hospital at Capital Medical University) for provision of FLAG-tagged WT FUS and FUS-R521C plasmids and Dr. Xiaochuan Wang (Tongji Medical College of Huazhong University of Science and Technology) for providing the GFP-tagged USP10 plasmid. This work was supported by the National Natural Science Foundation of China (82271642 to X.W. and 82171605 to S.Y.), the Natural Science Foundation of Hubei Province of China (2023AFB628 to X.W.), the Open Project of the NHC Key Laboratory of Male Reproduction and Genetics (Guangdong Provincial Reproductive Science Institute) (KF202005 to S.Y.), and the Basic Research Support Program of Huazhong University of Science and Technology (2023BR031 to S.Y.). This work was supported by the Cross Research Platform of Electromagnetics and Reproductive Health of Huazhong University of Science and Technology.

AUTHOR CONTRIBUTIONS

S.Y. and X.W. conceived and designed the research. X.W., X.F., J.Z., and F.W. performed the bench experiments. Y.W. established the knockout HeLa cell line. L.W., T.L., and J.C. carried out cell culture. H.G., Y.Z., and H.L. analyzed the data. X.W. wrote the manuscript. S.Y. revised the manuscript and supervised the project.

DECLARATION OF INTERESTS

The authors declare no competing interests.

Received: August 21, 2023
Revised: December 19, 2023
Accepted: January 25, 2024

REFERENCES

1. Bley, N., Lederer, M., Pfalz, B., Reinke, C., Fuchs, T., Glaß, M., Möller, B., and Hüttelmaier, S. (2015). Stress granules are dispensable for mRNA stabilization during cellular stress. Nucleic Acids Res. *43*, e26. https://doi.org/10.1093/nar/gku1275.
2. Mateju, D., Eichenberger, B., Voigt, F., Eglinger, J., Roth, G., and Chao, J.A. (2020). Single-Molecule Imaging Reveals Translation of mRNAs Localized to Stress Granules. Cell *183*, 1801–1812.e13. https://doi.org/10.1016/j.cell.2020.11.010.
3. Yang, P., Mathieu, C., Kolaitis, R.M., Zhang, P., Messing, J., Yurtsever, U., Yang, Z., Wu, J., Li, Y., Pan, Q., et al. (2020). G3BP1 Is a Tunable Switch that Triggers Phase Separation to Assemble Stress Granules. Cell *181*, 325–345.e28. https://doi.org/10.1016/j.cell.2020.03.046.
4. Sanders, D.W., Kedersha, N., Lee, D.S.W., Strom, A.R., Drake, V., Riback, J.A., Bracha, D., Eeftens, J.M., Iwanicki, A., Wang, A., et al. (2020). Competing Protein-RNA Interaction Networks Control Multiphase Intracellular Organization. Cell *181*, 306–324.e28. https://doi.org/10.1016/j.cell.2020.03.050.
5. Guillén-Boixet, J., Kopach, A., Holehouse, A.S., Wittmann, S., Jahnel, M., Schlüßler, R., Kim, K., Trussina, I.R.E.A., Wang, J., Mateju, D., et al. (2020). RNA-Induced Conformational Switching and Clustering of G3BP Drive Stress Granule Assembly by Condensation. Cell *181*, 346–361.e17. https://doi.org/10.1016/j.cell.2020.03.049.
6. Kedersha, N., Ivanov, P., and Anderson, P. (2013). Stress granules and cell signaling: more than just a passing phase? Trends Biochem. Sci. *38*, 494–506. https://doi.org/10.1016/j.tibs.2013.07.004.
7. Martin, J.L., Dawson, S.J., and Gale, J.E. (2022). An emerging role for stress granules in neurodegenerative disease and hearing loss. Hear. Res. *426*, 108634. https://doi.org/10.1016/j.heares.2022.108634.
8. Wolozin, B., and Ivanov, P. (2019). Stress granules and neurodegeneration. Nat. Rev. Neurosci. *20*, 649–666. https://doi.org/10.1038/s41583-019-0222-5.
9. Anderson, P., and Kedersha, N. (2009). RNA granules: post-transcriptional and epigenetic modulators of gene expression. Nat. Rev. Mol. Cell Biol. *10*, 430–436. https://doi.org/10.1038/nrm2694.
10. Gwon, Y., Maxwell, B.A., Kolaitis, R.M., Zhang, P., Kim, H.J., and Taylor, J.P. (2021). Ubiquitination of G3BP1 mediates stress granule disassembly in a context-specific manner. Science *372*, eabf6548. https://doi.org/10.1126/science.abf6548.
11. Maxwell, B.A., Gwon, Y., Mishra, A., Peng, J., Nakamura, H., Zhang, K., Kim, H.J., and Taylor, J.P. (2021). Ubiquitination is essential for recovery of cellular activities after heat shock. Science *372*, eabc3593. https://doi.org/10.1126/science.abc3593.
12. Markmiller, S., Fulzele, A., Higgins, R., Leonard, M., Yeo, G.W., and Bennett, E.J. (2019). Active Protein Neddylation or Ubiquitylation Is Dispensable for Stress Granule Dynamics. Cell Rep. *27*, 1356–1363.e3. https://doi.org/10.1016/j.celrep.2019.04.015.
13. Fang, M.Y., Markmiller, S., Vu, A.Q., Javaherian, A., Dowdle, W.E., Jolivet, P., Bushway, P.J., Castello, N.A., Baral, A., Chan, M.Y., et al. (2019). Small-Molecule Modulation of TDP-43 Recruitment to Stress Granules Prevents Persistent TDP-43 Accumulation in ALS/FTD. Neuron *103*, 802–819.e11. https://doi.org/10.1016/j.neuron.2019.05.048.
14. Dormann, D., and Haass, C. (2011). TDP-43 and FUS: a nuclear affair. Trends Neurosci. *34*, 339–348. https://doi.org/10.1016/j.tins.2011.05.002.
15. Li, Y.R., King, O.D., Shorter, J., and Gitler, A.D. (2013). Stress granules as crucibles of ALS pathogenesis. J. Cell Biol. *201*, 361–372. https://doi.org/10.1083/jcb.201302044.
16. David, C.J., Chen, M., Assanah, M., Canoll, P., and Manley, J.L. (2010). HnRNP proteins controlled by c-Myc deregulate pyruvate kinase mRNA splicing in cancer. Nature *463*, 364–368. https://doi.org/10.1038/nature08697.
17. Alarcón, C.R., Goodarzi, H., Lee, H., Liu, X., Tavazoie, S., and Tavazoie, S.F. (2015). HNRNPA2B1 Is a Mediator of m(6)A-Dependent Nuclear RNA Processing Events. Cell *162*, 1299–1308. https://doi.org/10.1016/j.cell.2015.08.011.
18. Villarroya-Beltri, C., Gutiérrez-Vázquez, C., Sánchez-Cabo, F., Pérez-Hernández, D., Vázquez, J., Martin-Cofreces, N., Martinez-Herrera, D.J., Pascual-Montano, A., Mittelbrunn, M., and Sánchez-Madrid, F. (2013). Sumoylated hnRNPA2B1 controls the sorting of miRNAs into exosomes through binding to specific motifs. Nat. Commun. *4*, 2980. https://doi.org/10.1038/ncomms3980.
19. Geissler, R., Simkin, A., Floss, D., Patel, R., Fogarty, E.A., Scheller, J., and Grimson, A. (2016). A widespread sequence-specific mRNA decay pathway mediated by hnRNPs A1 and A2/B1. Genes Dev. *30*, 1070–1085. https://doi.org/10.1101/gad.277392.116.
20. McKay, S.J., and Cooke, H. (1992). hnRNP A2/B1 binds specifically to single stranded vertebrate telomeric repeat TTAGGGn. Nucleic Acids Res. *20*, 6461–6464. https://doi.org/10.1093/nar/20.24.6461.
21. Fähling, M., Mrowka, R., Steege, A., Martinka, P., Persson, P.B., and Thiele, B.J. (2006). Heterogeneous nuclear ribonucleoprotein-A2/B1 modulate collagen prolyl 4-hydroxylase, alpha (I) mRNA stability. J. Biol. Chem. *281*, 9279–9286. https://doi.org/10.1074/jbc.M510925200.
22. Kosturko, L.D., Maggipinto, M.J., Korza, G., Lee, J.W., Carson, J.H., and Barbarese, E. (2006). Heterogeneous nuclear ribonucleoprotein (hnRNP) E1 binds to hnRNP A2 and inhibits translation of A2 response element mRNAs. Mol. Biol. Cell *17*, 3521–3533. https://doi.org/10.1091/mbc.e05-10-0946.
23. Wang, L., Wen, M., and Cao, X. (2019). Nuclear hnRNPA2B1 initiates and amplifies the innate immune response to DNA viruses. Science *365*, eaav0758. https://doi.org/10.1126/science.aav0758.
24. Kim, H.J., Kim, N.C., Wang, Y.D., Scarborough, E.A., Moore, J., Diaz, Z., MacLea, K.S., Freibaum, B., Li, S., Molliex, A., et al. (2013). Mutations in prion-like domains in hnRNPA2B1 and hnRNPA1 cause multisystem proteinopathy and ALS. Nature *495*, 467–473. https://doi.org/10.1038/nature11922.
25. Shorter, J., and Taylor, J.P. (2013). Disease mutations in the prion-like domains of hnRNPA1 and hnRNPA2/B1 introduce potent steric zippers that drive excess RNP granule assembly. Rare Dis. *1*, e25200. https://doi.org/10.4161/rdis.25200.
26. Guil, S., Long, J.C., and Cáceres, J.F. (2006). hnRNP A1 relocalization to the stress granules reflects a role in the stress response. Mol. Cell Biol. *26*, 5744–5758. https://doi.org/10.1128/MCB.00224-06.
27. Buchan, J.R., Kolaitis, R.M., Taylor, J.P., and Parker, R. (2013). Eukaryotic stress granules are cleared by autophagy and Cdc48/VCP function. Cell *153*, 1461–1474. https://doi.org/10.1016/j.cell.2013.05.037.
28. Yang, C., Wang, Z., Kang, Y., Yi, Q., Wang, T., Bai, Y., and Liu, Y. (2023). Stress granule homeostasis is modulated by TRIM21-mediated ubiquitination of G3BP1 and autophagy-dependent elimination of stress granules.

Autophagy *19*, 1934–1951. https://doi.org/10.1080/15548627.2022.2164427.

29. Bordi, M., Berg, M.J., Mohan, P.S., Peterhoff, C.M., Alldred, M.J., Che, S., Ginsberg, S.D., and Nixon, R.A. (2016). Autophagy flux in CA1 neurons of Alzheimer hippocampus: Increased induction overburdens failing lysosomes to propel neuritic dystrophy. Autophagy *12*, 2467–2483. https://doi.org/10.1080/15548627.2016.1239003.

30. Ma, T., Zhang, Y., Zhang, C., Luo, J.G., and Kong, L.Y. (2017). Downregulation of TIGAR sensitizes the antitumor effect of physapubenolide through increasing intracellular ROS levels to trigger apoptosis and autophagosome formation in human breast carcinoma cells. Biochem. Pharmacol. *143*, 90–106. https://doi.org/10.1016/j.bcp.2017.07.018.

31. Varga, R.E., Khundadze, M., Damme, M., Nietzsche, S., Hoffmann, B., Stauber, T., Koch, N., Hennings, J.C., Franzka, P., Huebner, A.K., et al. (2015). In Vivo Evidence for Lysosome Depletion and Impaired Autophagic Clearance in Hereditary Spastic Paraplegia Type SPG11. PLoS Genet. *11*, e1005454. https://doi.org/10.1371/journal.pgen.1005454.

32. Zhu, H., Yu, X., Zhu, S., Li, X., Lu, B., Li, Z., and Yu, C. (2015). The fusion of autophagosome with lysosome is impaired in L-arginine-induced acute pancreatitis. Int. J. Clin. Exp. Pathol. *8*, 11164–11170.

33. Hansen, T.E., and Johansen, T. (2011). Following autophagy step by step. BMC Biol. *9*, 39. https://doi.org/10.1186/1741-7007-9-39.

34. Poole, B., and Ohkuma, S. (1981). Effect of weak bases on the intralysosomal pH in mouse peritoneal macrophages. J. Cell Biol. *90*, 665–669. https://doi.org/10.1083/jcb.90.3.665.

35. Seglen, P.O., Grinde, B., and Solheim, A.E. (1979). Inhibition of the lysosomal pathway of protein degradation in isolated rat hepatocytes by ammonia, methylamine, chloroquine and leupeptin. Eur. J. Biochem. *95*, 215–225. https://doi.org/10.1111/j.1432-1033.1979.tb12956.x.

36. Mizushima, N., Yoshimori, T., and Levine, B. (2010). Methods in mammalian autophagy research. Cell *140*, 313–326. https://doi.org/10.1016/j.cell.2010.01.028.

37. Mauthe, M., Orhon, I., Rocchi, C., Zhou, X., Luhr, M., Hijlkema, K.J., Coppes, R.P., Engedal, N., Mari, M., and Reggiori, F. (2018). Chloroquine inhibits autophagic flux by decreasing autophagosome-lysosome fusion. Autophagy *14*, 1435–1455. https://doi.org/10.1080/15548627.2018.1474314.

38. Tolay, N., and Buchberger, A. (2021). Comparative profiling of stress granule clearance reveals differential contributions of the ubiquitin system. Life Sci. Alliance *4*, e202000927. https://doi.org/10.26508/lsa.202000927.

39. Turakhiya, A., Meyer, S.R., Marincola, G., Böhm, S., Vanselow, J.T., Schlosser, A., Hofmann, K., and Buchberger, A. (2018). ZFAND1 Recruits p97 and the 26S Proteasome to Promote the Clearance of Arsenite-Induced Stress Granules. Mol. Cell *70*, 906–919.e7. https://doi.org/10.1016/j.molcel.2018.04.021.

40. Kassouf, T., Shrivastava, R., Meszka, I., Bailly, A., Polanowska, J., Trauchessec, H., Mandrioli, J., Carra, S., and Xirodimas, D.P. (2023). Targeting the NEDP1 enzyme to ameliorate ALS phenotypes through stress granule disassembly. Sci. Adv. *9*, eabq7585. https://doi.org/10.1126/sciadv.abq7585.

41. Lagier-Tourenne, C., Polymenidou, M., and Cleveland, D.W. (2010). TDP-43 and FUS/TLS: emerging roles in RNA processing and neurodegeneration. Hum. Mol. Genet. *19*, R46–R64. https://doi.org/10.1093/hmg/ddq137.

42. Vance, C., Rogelj, B., Hortobágyi, T., De Vos, K.J., Nishimura, A.L., Sreedharan, J., Hu, X., Smith, B., Ruddy, D., Wright, P., et al. (2009). Mutations in FUS, an RNA processing protein, cause familial amyotrophic lateral sclerosis type 6. Science *323*, 1208–1211. https://doi.org/10.1126/science.1165942.

43. Suzuki, N., Aoki, M., Warita, H., Kato, M., Mizuno, H., Shimakura, N., Akiyama, T., Furuya, H., Hokonohara, T., Iwaki, A., et al. (2010). FALS with FUS mutation in Japan, with early onset, rapid progress and basophilic inclusion. J. Hum. Genet. *55*, 252–254. https://doi.org/10.1038/jhg.2010.16.

44. Yamamoto-Watanabe, Y., Watanabe, M., Okamoto, K., Fujita, Y., Jackson, M., Ikeda, M., Nakazato, Y., Ikeda, Y., Matsubara, E., Kawarabayashi, T., and Shoji, M. (2010). A Japanese ALS6 family with mutation R521C in the FUS/TLS gene: a clinical, pathological and genetic report. J. Neurol. Sci. *296*, 59–63. https://doi.org/10.1016/j.jns.2010.06.008.

45. Drepper, C., Herrmann, T., Wessig, C., Beck, M., and Sendtner, M. (2011). C-terminal FUS/TLS mutations in familial and sporadic ALS in Germany. Neurobiol. Aging *32*, 548.e1–548.e5484. https://doi.org/10.1016/j.neurobiolaging.2009.11.017.

46. Sproviero, W., La Bella, V., Mazzei, R., Valentino, P., Rodolico, C., Simone, I.L., Logroscino, G., Ungaro, C., Magariello, A., Patitucci, A., et al. (2012). FUS mutations in sporadic amyotrophic lateral sclerosis: clinical and genetic analysis. Neurobiol. Aging *33*, 837.e1–837.e8375. https://doi.org/10.1016/j.neurobiolaging.2011.10.005.

47. Zhang, X., Wang, F., Hu, Y., Chen, R., Meng, D., Guo, L., Lv, H., Guan, J., and Jia, Y. (2020). In vivo stress granule misprocessing evidenced in a FUS knock-in ALS mouse model. Brain *143*, 1350–1367. https://doi.org/10.1093/brain/awaa076.

48. Renu, K., Madhyastha, H., Madhyastha, R., Maruyama, M., Vinayagam, S., and Valsala Gopalakrishnan, A. (2018). Review on molecular and biochemical insights of arsenic-mediated male reproductive toxicity. Life Sci. *212*, 37–58. https://doi.org/10.1016/j.lfs.2018.09.045.

49. Kim, Y.J., and Kim, J.M. (2015). Arsenic Toxicity in Male Reproduction and Development. Dev. Reprod. *19*, 167–180. https://doi.org/10.12717/DR.2015.19.4.167.

50. Rachamalla, M., Chinthada, J., Kushwaha, S., Putnala, S.K., Sahu, C., Jena, G., and Niyogi, S. (2022). Contemporary Comprehensive Review on Arsenic-Induced Male Reproductive Toxicity and Mechanisms of Phytonutrient Intervention. Toxics *10*, 744. https://doi.org/10.3390/toxics10120744.

51. Wang, B., Maxwell, B.A., Joo, J.H., Gwon, Y., Messing, J., Mishra, A., Shaw, T.I., Ward, A.L., Quan, H., Sakurada, S.M., et al. (2019). ULK1 and ULK2 Regulate Stress Granule Disassembly Through Phosphorylation and Activation of VCP/p97. Mol. Cell *74*, 742–757.e8. https://doi.org/10.1016/j.molcel.2019.03.027.

52. Ganassi, M., Mateju, D., Bigi, I., Mediani, L., Poser, I., Lee, H.O., Seguin, S.J., Morelli, F.F., Vinet, J., Leo, G., et al. (2016). A Surveillance Function of the HSPB8-BAG3-HSP70 Chaperone Complex Ensures Stress Granule Integrity and Dynamism. Mol. Cell *63*, 796–810. https://doi.org/10.1016/j.molcel.2016.07.021.

53. Mediani, L., Antoniani, F., Galli, V., Vinet, J., Carrà, A.D., Bigi, I., Tripathy, V., Tiago, T., Cimino, M., Leo, G., et al. (2021). Hsp90-mediated regulation of DYRK3 couples stress granule disassembly and growth via mTORC1 signaling. EMBO Rep. *22*, e51740. https://doi.org/10.15252/embr.202051740.

54. Marmor-Kollet, H., Siany, A., Kedersha, N., Knafo, N., Rivkin, N., Danino, Y.M., Moens, T.G., Olender, T., Sheban, D., Cohen, N., et al. (2020). Spatiotemporal Proteomic Analysis of Stress Granule Disassembly Using APEX Reveals Regulation by SUMOylation and Links to ALS Pathogenesis. Mol. Cell *80*, 876–891.e6. https://doi.org/10.1016/j.molcel.2020.10.032.

55. Solomon, S., Xu, Y., Wang, B., David, M.D., Schubert, P., Kennedy, D., and Schrader, J.W. (2007). Distinct structural features of caprin-1 mediate its interaction with G3BP-1 and its induction of phosphorylation of eukaryotic translation initiation factor 2alpha, entry to cytoplasmic stress granules, and selective interaction with a subset of mRNAs. Mol. Cell Biol. *27*, 2324–2342. https://doi.org/10.1128/MCB.02300-06.

56. Kedersha, N., Panas, M.D., Achorn, C.A., Lyons, S., Tisdale, S., Hickman, T., Thomas, M., Lieberman, J., McInerney, G.M., Ivanov, P., and Anderson, P. (2016). G3BP-Caprin1-USP10 complexes mediate stress granule condensation and associate with 40S subunits. J. Cell Biol. *212*, 845–860. https://doi.org/10.1083/jcb.201508028.

57. Kwon, S., Zhang, Y., and Matthias, P. (2007). The deacetylase HDAC6 is a novel critical component of stress granules involved in the stress response. Genes Dev. *21*, 3381–3394. https://doi.org/10.1101/gad.461107.

58. Cui, Q., Bi, H., Lv, Z., Wu, Q., Hua, J., Gu, B., Huo, C., Tang, M., Chen, Y., Chen, C., et al. (2023). Diverse CMT2 neuropathies are linked to aberrant G3BP interactions in stress granules. Cell *186*, 803–820.e25. https://doi.org/10.1016/j.cell.2022.12.046.

59. Anderson, P., Kedersha, N., and Ivanov, P. (2015). Stress granules, P-bodies and cancer. Biochim. Biophys. Acta *1849*, 861–870. https://doi.org/10.1016/j.bbagrm.2014.11.009.

60. Zhang, P., Fan, B., Yang, P., Temirov, J., Messing, J., Kim, H.J., and Taylor, J.P. (2019). Chronic optogenetic induction of stress granules is cytotoxic and reveals the evolution of ALS-FTD pathology. Elife *8*, e39578. https://doi.org/10.7554/eLife.39578.

61. Mann, J.R., Gleixner, A.M., Mauna, J.C., Gomes, E., DeChellis-Marks, M.R., Needham, P.G., Copley, K.E., Hurtle, B., Portz, B., Pyles, N.J., et al. (2019). RNA Binding Antagonizes Neurotoxic Phase Transitions of TDP-43. Neuron *102*, 321–338.e8. https://doi.org/10.1016/j.neuron.2019.01.048.

62. Murakami, T., Qamar, S., Lin, J.Q., Schierle, G.S.K., Rees, E., Miyashita, A., Costa, A.R., Dodd, R.B., Chan, F.T.S., Michel, C.H., et al. (2015). ALS/FTD Mutation-Induced Phase Transition of FUS Liquid Droplets and Reversible Hydrogels into Irreversible Hydrogels Impairs RNP Granule Function. Neuron *88*, 678–690. https://doi.org/10.1016/j.neuron.2015.10.030.

63. Lee, K.H., Zhang, P., Kim, H.J., Mitrea, D.M., Sarkar, M., Freibaum, B.D., Cika, J., Coughlin, M., Messing, J., Molliex, A., et al. (2016). C9orf72 Dipeptide Repeats Impair the Assembly, Dynamics, and Function of Membrane-Less Organelles. Cell *167*, 774–788.e17. https://doi.org/10.1016/j.cell.2016.10.002.

64. Maharjan, N., Künzli, C., Buthey, K., and Saxena, S. (2017). C9ORF72 Regulates Stress Granule Formation and Its Deficiency Impairs Stress Granule Assembly, Hypersensitizing Cells to Stress. Mol. Neurobiol. *54*, 3062–3077. https://doi.org/10.1007/s12035-016-9850-1.

65. Wang, F., Wang, L., Gan, S., Feng, S., Ouyang, S., Wang, X., and Yuan, S. (2023). SERBP1 Promotes Stress Granule Clearance by Regulating 26S Proteasome Activity and G3BP1 Ubiquitination and Protects Male Germ Cells from Thermostimuli Damage. Research *6*, 0091. https://doi.org/10.34133/research.0091.

66. Cong, L., Ran, F.A., Cox, D., Lin, S., Barretto, R., Habib, N., Hsu, P.D., Wu, X., Jiang, W., Marraffini, L.A., and Zhang, F. (2013). Multiplex genome engineering using CRISPR/Cas systems. Science *339*, 819–823. https://doi.org/10.1126/science.1231143.

67. Wu, Y., Duan, P., Wen, Y., Zhang, J., Wang, X., Dong, J., Zhao, Q., Feng, S., Lv, C., Guo, Y., et al. (2022). UHRF1 establishes crosstalk between somatic and germ cells in male reproduction. Cell Death Dis. *13*, 377. https://doi.org/10.1038/s41419-022-04837-2.

STAR★METHODS

KEY RESOURCES TABLE

REAGENT or RESOURCE	SOURCE	IDENTIFIER
Antibodies		
hnRNP A2/B1 Antibody (B-7)	Santa Cruz Biotechnology	Cat#sc-374053; RRID:AB_10947257
VCP Monoclonal Antibody	Thermo Scientific	Cat#XG354371
TFEB Polyclonal Antibody	Thermo Scientific	Cat#A303-673A
Anti-Wilms Tumor Protein Antibody	abcam	Cat#AB89901; RRID:AB_2043201
Anti-ZFAND1 antibody	Sigma-Aldrich	Cat#HPA023383; RRID:AB_1859008
PABPC1 Rabbit pAb	ABclonal Technology	Cat#A14872; RRID:AB_2761752
NONO/p54nrb Rabbit pAb	ABclonal Technology	Cat#A21515
USP10 Rabbit mAb	ABclonal Technology	Cat#A4454; RRID:AB_2863277
Rabbit anti GFP-Tag mAb	ABclonal Technology	Cat#AE078
LC3A/B (D3U4C) XP® Rabbit mAb	Cell Signaling Technology	Cat#12741T; RRID:AB_2617131
Beclin-1 (D40C5) Rabbit mAb	Cell Signaling Technology	Cat#3495T; RRID:AB_1903911
Atg7 (D12B11) Rabbit mAb	Cell Signaling Technology	Cat#8558T; RRID:AB_10831194
Atg16L1 (D6D5) Rabbit mAb	Cell Signaling Technology	Cat#8089T; RRID:AB_10950320
Beta Tubulin Polyclonal antibody	Proteintech	Cat#10068-1-AP; RRID:AB_2303998
P62,SQSTM1 Polyclonal antibody	Proteintech	Cat#18420-1-AP; RRID:AB_10694431
FUS/TLS Polyclonal antibody	Proteintech	Cat#11570-1-AP; RRID:AB_2247082
TDP-43 Polyclonal antibody	Proteintech	Cat#10782-2-AP; RRID:AB_615042
TIAR Monoclonal antibody	Proteintech	Cat#66907-1-IG; RRID:AB_2882234
MYC tag Monoclonal antibody	Proteintech	Cat#60003-2-IG; RRID:AB_2734122
G3BP1 Polyclonal antibody	Proteintech	Cat#13057-2-AP; RRID:AB_2232034
VCP Polyclonal antibody	Proteintech	Cat#10736-1-AP; RRID:AB_2214635
G3BP2 Polyclonal antibody	Proteintech	Cat#16276-1-AP; RRID:AB_2878237
CAPRIN1 Polyclonal antibody	Proteintech	Cat#15112-1-AP; RRID:AB_2070016
USP10 Monoclonal antibody	Proteintech	Cat#67917-1-Ig; RRID:AB_2918671
MYC tag Polyclonal antibody	Proteintech	Cat#16286-1-AP; RRID:AB_11182162
GAPDH Monoclonal antibody	Proteintech	Cat#60004-1-Ig; RRID:AB_2107436
SFPQ Polyclonal antibody	Proteintech	Cat#15585-1-AP; RRID:AB_10697653
FMR1 Polyclonal antibody	Proteintech	Cat#13755-1-AP; RRID:AB_2262872
FXR1 Polyclonal antibody	Proteintech	Cat#13194-1-AP; RRID:AB_2110702
FAF2 Polyclonal antibody	Proteintech	Cat#16251-1-AP; RRID:AB_2262469
DYKDDDDK tag Polyclonal antibody	Proteintech	Cat#20543-1-AP; RRID:AB_11232216
GFP tag Polyclonal antibody	Proteintech	Cat#50430-2-AP; RRID:AB_11042881
HNRNPA1 Polyclonal antibody	Proteintech	Cat#11176-1-AP; RRID:AB_2117177
Ubiquitin Rabbit monoclonal antibody	Abcam	Cat#ab134953; RRID:AB_2801561
K48-ubiquitin Rabbit monoclonal antibody	Abcam	Cat#ab140601; RRID:AB_2783797
K63-ubiquitin Rabbit monoclonal antibody	Abcam	Cat#ab179434; RRID:AB_2895239
Mouse IgG	Proteintech	Cat#B900620; RRID:AB_2883054
Rabbit IgG	Proteintech	Cat#30000-0-AP; RRID:AB_2819035
HRP-conjugated Anti-Heavy Chain of Rabbit IgG	Proteintech	Cat#SA00001-7H; RRID:AB_2935611
HRP, Goat Anti-Rabbit IgG	Abbkine	Cat#A21020; RRID:AB_2876889
HRP, Goat Anti-Mouse IgG	Abbkine	Cat#A21010; RRID:AB_2728771
HRP, Mouse Anti-Rabbit IgG LCS	Abbkine	Cat#A25022; RRID:AB_2893334
HRP, Goat Anti-Rabbit IgG HCS	Abbkine	Cat#A25222; RRID:AB_2922982

(*Continued on next page*)

Continued

REAGENT or RESOURCE	SOURCE	IDENTIFIER
HRP, Goat Anti-Mouse IgG LCS	Abbkine	Cat#A25012; RRID:AB_2737290
HRP, Goat Anti-Mouse IgG HCS	Abbkine	Cat#A25112; RRID:AB_2922983
Goat Anti-Rabbit IgG H&L (Alexa Fluor® 488)	abcam	Cat#ab150077; RRID:AB_2630356
Goat Anti-Mouse IgG H&L (Alexa Fluor® 488)	abcam	Cat#ab150113; RRID:AB_2576208
Goat Anti-Rabbit IgG H&L (Alexa Fluor® 594)	abcam	Cat#ab150080; RRID:AB_2650602
Goat Anti-Mouse IgG H&L (Alexa Fluor® 594)	abcam	Cat#ab150116; RRID:AB_2650601
Bacterial and virus strains		
DH5α Chemically Competent Cell	Tsingke	Cat#TSC-C14
Chemicals, peptides, and recombinant proteins		
BbsI	NEB	Cat#R3539
NaAsO2	Sigma-Aldrich	Cat#S7400
D-Sorbitol	Sinopharm	Cat#63011034
NaCl	Sinopharm	Cat#10019318
BTZ	Selleckchem	Cat#S1013
CB-5083	Selleckchem	Cat#S8101
TAK-243	Selleckchem	Cat#S8341
protease inhibitor cocktail	MCE	Cat#HY-K0010
MG-132	MCE	Cat#HY-13259
Critical commercial assays		
DMEM	Procell	Cat#PM150210
FBS	ABW	Cat#AB-FBS-1050S
penicillin/streptomycin	Beyotime	Cat#C0222
Lipo8000	Beyotime	Cat#C0533
INTERFERin	VWR	Cat#89129–932
PBS	Servicebio	Cat#G4202
IP lysis buffer	Beyotime	Cat#P0013
protein A/G magnetic beads	MCE	Cat#HY-K0202
RNase A	Beyotime	Cat#ST578
5×SDS-PAGE protein loading buffer	Yeasen	Cat#20315ES20
skim milk	Biosharp	Cat#BS102
ECL reagent mixture	Bio-Rad	Cat#1705061
antifade mounting medium	Abbkine	Cat#BMU104-CN
Bouin's solution	Sigma-Aldrich	Cat#HT10132
Periodic Acid-Schiff Staining Kit	Beyotime	Cat#C0142S
O.C.T.	Sakura Finetek	Cat#4583
Deposited data		
List of hnRNPA2B1-interacting proteins identified by IP-MS	This paper	jPOST: JPST002463 PXID:PXD048539
Experimental models: Cell lines		
HeLa	Laboratory of Shuiqiao Yuan	N/A
Experimental models: Organisms/strains		
floxed-Hnrnpa2b1 mice	Cyagen Biosciences (Suzhou) Inc	S-CKO-11602
Oligonucleotides		
HNRNPA2B1-Gene knockout-sgRNA1: CAAGACCTCATTCAATTGAT	ShangHai Sangon Biotech	N/A
HNRNPA2B1-Gene knockout-sgRNA2: TGGCTGAGGTTGATGCTGCC	ShangHai Sangon Biotech	N/A

(*Continued on next page*)

Continued

REAGENT or RESOURCE	SOURCE	IDENTIFIER
HNRNPA2B1-Genotyping of KO HeLa cell-Forward: CATGGAGGAAATAACTATCAG	ShangHai Sangon Biotech	N/A
HNRNPA2B1-Genotyping of KO HeLa cell-Reverse: CAACAATATTAAGCAGCTTC	ShangHai Sangon Biotech	N/A
TFEB-Gene knockdown-siRNA1(605): GAACAAGUUUGCUGCCCACAUTT	ShangHai Sangon Biotech	N/A
TFEB-Gene knockdown-siRNA2(1037): GAGACGAAGGUUCAACAUCAATT	ShangHai Sangon Biotech	N/A
SQSTM1(p62)-Gene knockdown-siRNA1(272): CGAGGAAUUGACAAUGGCCAUTT	ShangHai Sangon Biotech	N/A
SQSTM1(p62)-Gene knockdown-siRNA2(371): CCGAAUCUACAUUAAAGAGAATT	ShangHai Sangon Biotech	N/A
HNRNPA1-Gene knockdown-siRNA1(399): AGAUAUUUGUUGGUGGCAUUATT	ShangHai Sangon Biotech	N/A
HNRNPA1-Gene knockdown-siRNA2(668): CGAAGUGGUUCUGGAAACUUUTT	ShangHai Sangon Biotech	N/A
USP10-Gene knockdown-siRNA1: CCAUAAAGAUUGCAGAGUUTT	ShangHai Sangon Biotech	N/A
USP10-Gene knockdown-siRNA2: CAAACAAGAGGUUGAGAUATT	ShangHai Sangon Biotech	N/A
Recombinant DNA		
hnRNPA2-FL-Plasmid construction-Forward: GTCGAATTCGGATGGAGAGAGAAAAGGAACAGT	ShangHai Sangon Biotech	N/A
hnRNPA2-FL-Plasmid construction-Reverse: GATCTCGAGGTATCGGCTCCTCCCACCATAAC	ShangHai Sangon Biotech	N/A
hnRNPA2-N-Term-Plasmid construction-Forward: GTCGAATTCGGATGGAGAGAGAAAAGGAACAGT	ShangHai Sangon Biotech	N/A
hnRNPA2-N-Term-Plasmid construction-Reverse: GATCTCGAGTTGTCTAGACAAAGCCTTTC	ShangHai Sangon Biotech	N/A
hnRNPA2-RRM1-Plasmid construction-Forward: GTCGAATTCGGATGGAGAGAGAAAAGGAACAGT	ShangHai Sangon Biotech	N/A
hnRNPA2-RRM1-Plasmid construction-Reverse: GATCTCGAGTCTTGCTACAGCACGTTTTGGC	ShangHai Sangon Biotech	N/A
hnRNPA2-RRM2-Plasmid construction-Forward: GTCGAATTCGGAAGAAGCTGTTTGTTGGCGGAA	ShangHai Sangon Biotech	N/A
hnRNPA2-RRM2-Plasmid construction-Reverse: GATCTCGAGTTGTCTAGACAAAGCCTTTC	ShangHai Sangon Biotech	N/A
hnRNPA2-C-Term-Plasmid construction-Forward: GTCGAATTCGGGAAATGCAGGAAGTTCAGAGTT	ShangHai Sangon Biotech	N/A
hnRNPA2-C-Term-Plasmid construction-Reverse: GATCTCGAGGTATCGGCTCCTCCCACCATAAC	ShangHai Sangon Biotech	N/A
hnRNPA2-D290V-Plasmid construction-Forward1: GTCGAATTCGGATGGAGAGAGAAAAGGAACAGT	ShangHai Sangon Biotech	N/A
hnRNPA2-D290V-Plasmid construction-Reverse1: CATTGTAATTTCCACTTCCATAA	ShangHai Sangon Biotech	N/A
hnRNPA2-D290V-Plasmid construction-Reverse2: GCTGGTTATAATTTCCAAAAACATTGTAATTTCC ACTTCCATAA	ShangHai Sangon Biotech	N/A
hnRNPA2-D290V-Plasmid construction-Forward2: TTTTGGAAATTATAACCAGCAAC	ShangHai Sangon Biotech	N/A
hnRNPA2-D290V-Plasmid construction-Reverse3: GATCTCGAGGTATCGGCTCCTCCCACCATAAC	ShangHai Sangon Biotech	N/A

(*Continued on next page*)

Continued

REAGENT or RESOURCE	SOURCE	IDENTIFIER
Hnrnpa2b1-KO-Genotyping of KO mice-Forward: ATTTCGTTGTGCAGTCATAGGTCC	ShangHai Sangon Biotech	N/A
Hnrnpa2b1-KO-Genotyping of KO mice-Reverse1: CATGAAGAATGCTGAAACTCCAGA	ShangHai Sangon Biotech	N/A
Hnrnpa2b1-KO-Genotyping of KO mice-Reverse2: TCCTGCAGCTTGTTACCAATTACT	ShangHai Sangon Biotech	N/A
Software and algorithms		
Metascape	https://metascape.org/	N/A
STRING	https://cn.string-db.org/	N/A
Photoshop	Adobe	N/A
Prism	GraphPad	N/A
ImageJ	NIH	N/A
Biorender	https://app.biorender.com/	N/A

RESOURCE AVAILABILITY

Lead contact

Further information and requests for resources and reagents should be directed to and will be fulfilled by the lead contact, Dr. Shuiqiao Yuan (shuiqiaoyuan@hust.edu.cn).

Materials availability

Reagents describe in this paper are available from the lead contact upon request with a completed Material Transfer Agreement.

Data and code availability

- IP-MS data have been deposited at jPOST (JPST002463) and are publicly available.
- All data reported in this paper will be shared by the lead contact upon request.
- This paper does not report original code.
- Any additional information required to reanalyze the data reported in this work paper is available from the lead contact upon request.

EXPERIMENTAL MODEL AND STUDY PARTICIPANT DETAILS

Generation of *Hnrnpa2b1* gene knockout mice

Hnrnpa2b1 global knockout (KO) mice were created using Cre/*LoxP* breeding strategy. In brief, floxed-*Hnrnpa2b1* mice (Cat# S-CKO-11602) purchased from Cyagen Biosciences (Suzhou) Inc. were bred with Vasa-Cre mice to generate Vasa-Cre, *Hnrnpa2b1*$^{+/flox}$ males, and the male Vasa-Cre, *Hnrnpa2b1*$^{+/flox}$ mice were further crossed with wild-type (WT) female mice to obtain *Hnrnpa2b1*$^{+/-}$ heterozygous mice. Then, the *Hnrnpa2b1*$^{+/-}$ males were bred with *Hnrnpa2b1*$^{+/-}$ females to generate the *Hnrnpa2b1*$^{-/-}$ (designated as *Hnrnpa2b1* KO) males. The PCR primer sequences for genotyping are listed in the key resources table in the STAR Methods.

hnRNPA2B1 knockout HeLa cell line generation

hnRNPA2B1 genomic locus editing was mediated by CRISPR/Cas9 D10A nickase, two specific sgRNAs (sgRNA1: 5′-CAAGACCTCATTCAATTGAT-3’; sgRNA2: 5′-TGGCTGAGGTTGATGCTGCC-3′) targeting exon 4 were ligated into BbsI (NEB: R3539) digested pX335 vector according to the previous description,[66] then HeLa cells were co-transfected with pX335-sgRNA1 and pX335-sgRNA2 plasmids for 36 h and single-cell clones were seeded into 96-well plates. Individual clones were expanded, tested by DNA sequencing of a PCR amplicon spanning the predicted Cas9 cleavage site, and further confirmed by the TA clone. Clones with disruptive indels in both *hnRNPA2B1* alleles were then tested by western blot for the hnRNPA2B1 protein level. *hnRNPA2B1* knockout of HeLa cell line was performed in the Cell Laboratory, Institute of Reproductive Health, Tongji Medical College, Huazhong University of Science and Technology, by X.W and Y.W.

Mice

All mice used in this study were C57BL/6J gene background, and raised in a pathogen-free mouse house in the Animal Center of Tongji Medical College, Huazhong University of Science and Technology. All animal work was performed and approved by the Institutional Animal Care and Use Committee (IACUC) of Huazhong University of Science and Technology. J.Z. was responsible for the feeding of

mice. Male mice of a specific age from 0 days after birth to adulthood were selected for phenotypic analysis, and male mice of postnatal 8–10 day were selected for Sertoli cell isolation.

METHOD DETAILS

Plasmids and siRNA construction

For the generation of hnRNPA2B1 variants, PCR-amplified sequences were ligated into the pCMV-Myc vector. FLAG-tagged WT FUS and FUS-R521C plasmids were kindly gifts from Dr. Juanjuan Gong in Beijing Children's Hospital at Capital Medical University. GFP-tagged USP10 plasmid were kindly gifts from Dr. Xiaochuan Wang in Tongji Medical College of Huazhong University of Science and Technology. siRNAs against human *TFEB*, *p62, hnRNPA1* and *USP10* were purchased from Sangon Biotech (Shanghai) with sequences listed in the key resources table in the STAR Methods.

Cell culture and transfection

HeLa cells were cultured in DMEM (Procell, PM150210) supplemented with 10% fetal bovine serum (FBS, ABW, AB-FBS-1050S) and 1% penicillin/streptomycin (Beyotime, C0222) in a humidified incubator at 37°C with 5% CO_2. For transfection, Lipo8000 (Beyotime, C0533) was used for plasmid transfection and INTERFERin (VWR, 89129-932) was applied for siRNA transfection separately according to the experimental method provided by the manufacturer. Studies were conducted using MG-132(10 μM, MCE, HY-13259), which was treated 4 h before harvesting cells.

Arsenite treatment, heat shock and drug treatments

Stress granules were induced by adding $NaAsO_2$ (Sigma-Aldrich, S7400), D-Sorbitol (0.4 M, Sinopharm, 63011034), and NaCl (0.2 M, Sinopharm,10019318) into the cell culture medium for 1 h in a humidified incubator at 37°C with 5% CO_2. For heat shock induction, cells were transferred to a humidified incubator at 43°C with 5% CO_2 for 1 h. For drug inhibition, the cells were pretreated with Bafilomycin A1 (200 nM, Sangon Biotech, A601116) for 6 h, chloroquine (40 μM, Sigma-Aldrich, 50-63-5) for 6 h, BTZ (5 μM, Selleckchem, S1013) for 25 min, CB-5083 (5 μM, Selleckchem, S8101) for 6 h, and TAK-243 (1 μM, Selleckchem, S8341) for 25 min, respectively, followed by SG induction with arsenite for 1 h and recovery for up to 2.5 h in the continued presence of the drugs, with DMSO as a negative control.

Immunoprecipitation

Cells were rinsed with PBS (Servicebio, G4202), scraped off with a cell scraper (NEST, 710011), and lysed with IP lysis buffer (Beyotime, P0013) supplemented with protease inhibitor cocktail (MCE, HY-K0010). After centrifuge, cell supernatants were incubated with primary antibodies or normal IgG conjugated with protein A/G magnetic beads (MCE, HY-K0202) at 4°C overnight. RNase A digestions were carried out by adding RNase A (Beyotime, ST578) to cell lysates at a final concentration of 20 μg/mL, followed by 30 min incubation at room temperature (RT). Beads were washed five times with lysis buffer and the eluted proteins were diluted by 5×SDS-PAGE protein loading buffer (Yeasen, 20315ES20). The obtained samples were analyzed by western blotting.

Mass spectrometry

After the target protein Co-IP experiment, the obtained protein was enzymolysis, and then the peptide concentration was determined by OD280 for LC-MS analysis. During LC-MS/MS analysis, appropriate peptide segments were taken for chromatographic separation using the Easy nLC 1200 chromatographic system (Thermo Scientific) with nanoliter flow rate, and samples were injected into Trap Column (100μm*20mm, 5μm, C18). The chromatographic column (75μm*150mm, 3μm, C18, Dr. Maisch GmbH) was then used for gradient separation. The peptide was isolated and then analyzed by DDA (Data-dependent Acquisition) mass spectrometry using Q-Exactive mass spectrometer (Thermo Scientific). MaxQuant database was used for retrieval, and then experimental results and data analysis were carried out.

Western blotting

Cells were washed twice with cold PBS, suspended in lysis buffer (Beyotime, P0013), followed by adding the appropriate amount of 5×sample buffer (Yeasen, 20315ES20) to 1× and denatured at 98°C for 10 min. Proteins were separated by 10% SDS-PAGE and transferred onto polyvinylidene difluoride membranes (Millipore, IPVH00010). The membrane was blocked with 10% skim milk (Biosharp, BS102) in TBST (50 mM Tris-Cl, pH 7.5, 150 mM NaCl, 0.1% Tween 20) for 1 h at RT and incubated with the indicated primary antibodies in blocking solution at 4°C overnight on a shaker. After three times washing (10 min each) with TBST, the membranes were incubated with HRP-conjugated secondary antibody in TBST for 1.5 h at RT, rewashed three times with TBST, and incubated with ECL reagent mixture (Bio-Rad, 1705061) and visualized using ChemiDoc XRS+ system (Bio-Rad). The antibodies used are listed in the key resources table in the STAR Methods.

Immunofluorescence of cells

Cells were seeded to 70% confluence on circular coverslips in a 24-well plate for 24 h before treatment. Cells were then fixed in 4% paraformaldehyde (PFA) for 15 min at RT, infiltrated with 0.25% Triton X-100 in PBS for 10 min, and blocked with 5% BSA for 1 h at

RT. After incubation with a primary antibody in 5% BSA overnight at 4°C, cells were washed three times (10 min each) with PBS, incubated with a fluorophore-coupled secondary antibody for 2 h at RT, dyed with 4′,6-diamidino-2-phenylindole (DAPI), rewashed with PBS three times, mounted with antifade mounting medium (Abbkine, BMU104-CN) and sealed with nail polish. Images were obtained using a confocal microscope LSM900 (Zeiss).

Histological analysis and immunostaining of testis

Mouse testes from WT and *Hnrnpa2b1* KO mice were fixed in Bouin's solution (Sigma-Aldrich, HT10132) or 4% PFA at 4°C overnight for histology or immunostaining. For histological analysis, samples were embedded in paraffin and sectioned (5 μm-thick) using a Scientific CryoStar NX50 cryostat (ThermoFisher). Paraffin sections were subjected to PAS staining using Periodic Acid-Schiff Staining Kit (Beyotime, C0142S) following the manufacturer's instructions. For immunostaining, PFA-fixed testes were processed with gradient sucrose, embedded in O.C.T. (Sakura Finetek, 4583), sectioned (5 μm-thick), and subjected to antigen retrieval in a microwave oven with 0.01 M sodium citrate buffer (pH = 6.0). After blocking in 1% BSA supplemented with 5% normal donkey serum and 5% FBS for 1 h at RT, samples were incubated with primary antibodies in a blocking solution at 4°C overnight. Then, the samples were incubated with fluorophore-coupled secondary antibodies for 2 h at RT after washing 3 times (10 min each) and dyed with 4′,6-diamidino-2-phenylindole (DAPI). Images were captured using a confocal microscope LSM900 (Zeiss).

Sertoli cell purification

Sertoli cells were isolated as described previously with minor modifications.[67] In brief, after removing tunica albuginea, the testes (postnatal day 8–10) were digested with collagenase IV (1 mg/mL) at 37°C for 10 min, centrifuged at 70 g for 1 min at RT to remove Leydig/interstitial cells and resuspended with PBS. Subsequently, seminiferous tubules were incubated with 0.25% Trypsin and DNase I (0.5 mg/mL) for 3 min at 37°C in the shaker, added an equal volume of DMEM/F12 containing 10% FBS (called complete F12 medium) to terminate digestion and centrifuged at 1000 rpm for 3 min. After discarding the supernatant, the mixture containing SCs was resuspended with F12 medium and filtered with 40 μm pore-size nylon mesh. The obtained pellet was suspended and cultured in F12 medium at 35°C with 5% CO_2 for 30 min, then the medium with non-adherent germ cells was removed, and the remained Sertoli cells were grown in F12 medium for subsequent experiments.

Fluorescence recovery after photo bleaching

FRAP measurements were performed with the LSM900 Confocal Microscope (Zeiss). WT and hnRNPA2B1 KO cells were seeded into glass-bottom cell culture dish (NEST, Cat. 801001) and were transfected with GFP-G3BP1 plasmids the next day. 14 h later, cells were incubated with 0.5 mM arsenite for 30min. Photobleaching of SGs occurred 6s into capture, using the 488-nm FRAP laser to bleach the green channel. Data was analyzed in ImageJ employing the FRAP plugin, specific regions of interest (ROIs) were generated in the photobleach region, a nonphotobleached cell, and the background for each time-lapse, and the mean fluorescent intensity of each was extracted. These values were exported into GraphPad Prism, where fit FRAP curves were generated.

QUANTIFICATION AND STATISTICAL ANALYSIS

All data are presented as Mean ± S.E.M. unless otherwise noted in the figure legends. Statistical differences between datasets were assessed using a two-tailed Student's t-test, and p-values were denoted in figures by *$p < 0.05$; **$p < 0.01$; ***$p < 0.001$. Go ontology and protein-protein interaction network were analyzed online by using Metascape (https://metascape.org/) or STRING (https://cn.string-db.org/). Images and data quantitation were processed by Photoshop or GraphPad Prism software, respectively. Graphical abstract was created with BioRender.com.